2017

Lunar Laser Ranging: Testing Gravitation to the Moon and Back

Else Schlerman
eschlerm@wellesley.edu

Lunar Laser Ranging: Testing Gravitation to the Moon and Back

by

Else Schlerman

Submitted to the Department of Physics
in partial fulfillment of the requirements for the degree of

Bachelor of Arts in Physics

at

WELLESLEY COLLEGE

May 2017

Author .....
Department of Physics
April 21, 2017

Certified by .....
James Battat
Assistant Professor
Thesis Supervisor

Accepted by .....
Glenn Stark
Chair, Department of Physics

Lunar Laser Ranging: Testing Gravitation to the Moon and Back

by

Else Schlerman

Submitted to the Department of Physics
on April 21, 2017, in partial fulfillment of the
requirements for the degree of
Bachelor of Arts in Physics

Abstract

Capable of testing Einstein's theory of General Relativity, Lunar Laser Ranging measures the orbit of the Moon around the Earth by pulsing laser light from a telescope on Earth to five passive lunar reflectors placed on the Moon by Apollo astronauts and Russian rovers. One such operation, APOLLO (the Apache Point Observatory Lunar Laser-ranging Operation) has achieved millimeter precision measurements of the Earth-Moon distance, allowing for 10 times more stringent constraints of gravitational parameters. Until recently, however, there was no way to assess the measurement accuracy. In order to test gravitational models with greater accuracy, APOLLO implemented the Absolute Calibration System (ACS), an internal calibration laser, which pulses light at a frequency stable at the part per trillion level. My thesis research centered around making improvements to one component of the ACS, the Laser Slicer Board (LSB), which acts as a very fast ON/OFF gate for light from the ACS calibration laser. In preparation for this work, I redesigned the Opto-isolation and Tiltmeter Board (opto-tilt board) for APOLLO, replacing a previous opto-isolation board that had not been electrically functioning and combining it with an accelerometer-based tiltmeter to conserve space. After developing the schematic and layout of this board, I populated, tested, and installed the board at Apache Point Observatory in January 2017. As a theoretical exercise, I also took advantage of the time measurements from APOLLO's two clocks – one GPS-disciplined to behave as if it were at sea level and the other counting time at an altitude of 2.8 km – to explore the phenomena of Gravitational Redshift and its effects on measuring time.

Thesis Supervisor: James Battat
Title: Assistant Professor

Acknowledgments

I would like to thank my thesis advisor, Profesor James Battat, for his dedication, guidance, and support. I am grateful to him not only for encouraging me to thesis this year, but also for making it an incredibly enjoyable and rewarding experience.

I am also grateful to my thesis committee, Professors Glenn Stark, Robbie Berg, and Anjeana Hans, for their time and consideration.

Furthermore, my thesis would have been all the more difficult without my family and their continual support throughout this process. From discussions about the best circuit mounting setup at dinner to the most recent string of care packages (chocolate, homemade cookies, and an Arduino for good measure), thank you for helping me through my biggest school project yet.

Contents

List of Figures

List of Tables

Chapter 1

Introduction

1.1 Motivations

Even though gravity has a continuous impact on our daily lives, it remains a phenomenon that is still not very well understood. Newton's Law of Universal Gravitation, $F = GMm/r^2$, has been widely accepted and tested as a means of describing gravitational force for centuries. However, Newton's Law provides no explanation for why there is an attraction between masses, nor how one mass seemingly instantaneously applies a force on another mass, even across large expanses of empty space. Instead, it simply allows us to determine this attractive force. Additionally, there arise discrepancies between Newtonian predictions and observations, in particular in the trajectory of the planet Mercury [10]. With Einstein's development of the theory of General Relativity (GR) in the early 1900s, Newton's gravitational force was put into question. Einstein instead suggested that gravity is not an attraction force, but rather the effect of a curvature in spacetime resulting from mass or energy [10]. This theory adjusted the theoretical orbit of Mercury to match the observed better than Newtonian gravity, and GR predictions such as black holes have since been astronomically discovered [10]. In the theory of GR, Einstein argued that accelerations of massive objects in the geometry of spacetime are transmitted via gravitational waves traveling at the speed of light [11]. The recent discovery of these gravitational waves further supports the place of GR as a frontrunner amongst gravitational models.

However, physicists must now contend with the incompatibility of GR and Quantum Mechanics (QM). In particular, the standard model of quantum field theory, bridging the gap between Special Relativity and QM, does not include gravity, yet has been shown to hold at far higher precision than GR [10]. Exploring various models of gravity and how they deviate from one another can lead to better understanding of how different models of our universe, perhaps once thought to be incompatible, can merge.

Compared to the other three fundamental forces, the strong, electromagnetic, and weak forces, gravity is extremely weak. This makes high precision tests of gravitational models difficult. Studying it in a lab-environment is particularly challenging due to the small size of the masses in question relative to these other forces. To put this into perspective, the hydrogen atom's negatively-charged electron, e^-, and positively-charged proton, p^+, are bound by electrostatic forces, giving the atom the size of 0.1 nm. If gravity were the sole binding force between the two masses a single hydrogen atom would be larger than the size of the observable universe. Those studying gravitational waves, such as scientists at the Laser Interferometer Gravitational-Wave Observatory (LIGO), face similar issues in scale. Attempting to detect for waves with a miniscule strain (the fractional change in length) on the order of 10^{-21}, scientists at LIGO needed to build a Michelson interferometer with 4 km long arms [11]. However, on an astronomical scale the effects of gravity become easier to isolate due to both the large masses present in our universe and the relatively small influence of other forces on those masses.

1.2 Lunar Laser Ranging

One particularly powerful way of experimentally analyzing gravity using astronomical systems is through Lunar Laser Ranging (LLR). First conceived by R.H. Dicke in the 1950s, LLR involves taking high precision measurements of the Moon's orbit around the Earth through targeted short pulses of light from a laser on Earth. Although both Massachusetts Institute of Technology and the Soviet Crimean Observatory at-

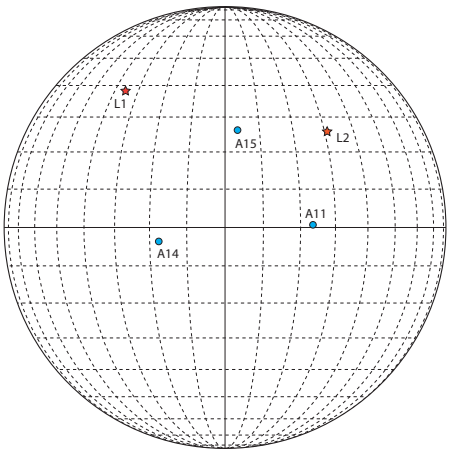

Figure 1-1: Positions of five passive corner cube retroreflector arrays on the Moon's surface. Figure from [1].

tempted early LLR experiments after the invention of lasers in the early 1960s, the scattering of the photons on the Moon's surface prevented any clear return signal. It was only with the first installation of a corner cube retroreflector array on the Moon during the 1969 Apollo 11 mission that LLR began to see successes, starting at the Lick Observatory in California using their 3.1 m telescope. Long-term LLR efforts subsequently began at the McDonald Observatory in Texas and the Crimean Astrophysical Observatory. While several observatories have demonstrated LLR capability, the McDonald Observatory has a significant operation due to its long term data collection from 1969 to present. In the 1980s, interest in LLR was rekindled, during which time the LLR operation at McDonald Observatory moved to a 0.76 m telescope exclusively for laser ranging, both lunar and satellite, and was renamed the McDonald Laser Ranging System (MLRS). Since 1984, France's Observatoire de la Côte d'Azur (OCA) has become leading LLR operation as well. Currently, the Apache Point Observatory Lunar Laser-ranging Operation (APOLLO, discussed in Section 1.3) and OCA are the two foremost LLR operations in the world, while MLRS is no longer as strong a contributor. Matera Laser Ranging Station in Italy and the Wettzell Laser Ranging System in Germany have LLR capabilities as well [1, 2].

Today, the laser pulses reflect off of one of five passive corner cube retroreflector arrays on the Moon's surface. In the early 1970s following the successful Apollo 11

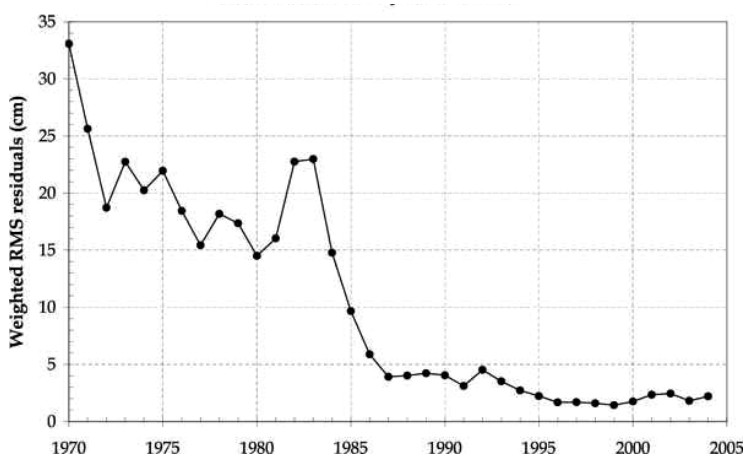

Figure 1-2: Historical accuracy of LLR measurements. Figure from [2].

mission, US astronauts installed two more arrays during Apollo 14 and 15 missions, while the remaining two French-made reflectors are mounted on the now-stationary Soviet lunar rovers, Lunokhod 1 and 2. The positions of these arrays on the Moon's surface are shown Figure 1-1, with A demarcating Apollo-installed retroreflectors and L, the two Lunokhod rovers. The Apollo 11 and 14 arrays each consist of 100 fused-silica reflectors (3.8 cm diameter), while the Apollo 15 array significantly has 300. The French reflectors on Lunokhod 1 and 2 are triangular (11 cm edge length), with 14 reflectors per array, and thought to have reflecting capabilities somewhere between the Apollo 11/14 and Apollo 15 arrays [1]. Using these retroreflectors, the distance between the Earth and Moon can be determined by measuring the travel time of the photons from Earth to Moon and back again. Over the course of the year, these distances range from 351,000 km to 406,000 km, or photon travel times of 2.34 s to 2.71 s [1]. Starting with a precision of around 35 cm for the Earth-Moon distance at McDonald Observatory in 1969, LLR has seen great improvements over the past 48 years with the recent achievement of millimeter precision by the APOLLO project. Figure 1-2 shows the historical accuracy of LLR measurements in terms of residuals from data-model comparison [12, 1].

Precise knowledge of the lunar orbit enables better understanding of the gravitational interactions of the Earth-Moon-Sun system, in particular facilitating the evaluation of different theories of gravitation and their deviation from experimental

data. Using LLR, scientists can constrain certain parameters of parameterized post-Newtonian (PPN) formalism, providing information about what theories of gravity best fit the data. This way, LLR tests the weak equivalence principle (WEP), the strong equivalence principle (SEP), the time-rate-of-change of the gravitational constant $\dot{G}/G$, geodetic precession, and gravitomagnetism. Information about the orbit of the Moon also allows for better understanding of the structure of the Moon itself. For instance, LLR supports the presence of a liquid lunar core about 350 km deep. Additionally, data from LLR provide information on the libration of the Moon due to its tidal interactions with the Earth [1].

1.3 APOLLO

My work for this thesis was done in collaboration with the Apache Point Observatory Lunar Laser-ranging Operation or APOLLO. APOLLO is unique among LLR groups due to its achievement of precision in the millimeter range, or a part in a trillion of the Earth-Moon distance, since 2006 [12]. These observations have constrained gravitational theories a further order of magnitude. As of September 2013, APOLLO has measured:

- SEP: to $\eta \approx 3 \times 10^{-4}$ sensitivity [1]
- WEP: to $\Delta a/a > 1.3 \times 10^{-13}$ sensitivity [1]
- Time-rate-of-change of gravitational constant constrained to $\dot{G}/G < 10^{-12}\,\mathrm{yr}^{-1}$ [1]

What makes APOLLO unique among LLR operations come from a few factors. APOLLO is located at New Mexico's Apache Point Observatory (APO) at an altitude of 2788 m, and makes use of the large aperture of the telescope (3.5 m) and particularly good atmospheric "seeing" at APO. The APOLLO Nd:YAG laser produces 100 ps pulses (about a few centimeters thick) of 1064 nm wavelength light, which is then frequency doubled to $\lambda = 532\,\mathrm{nm}$, at a rate of 20 Hz [1, 13]. A small fraction of this outgoing pulse is redirected by a local corner cube back to the detector. This

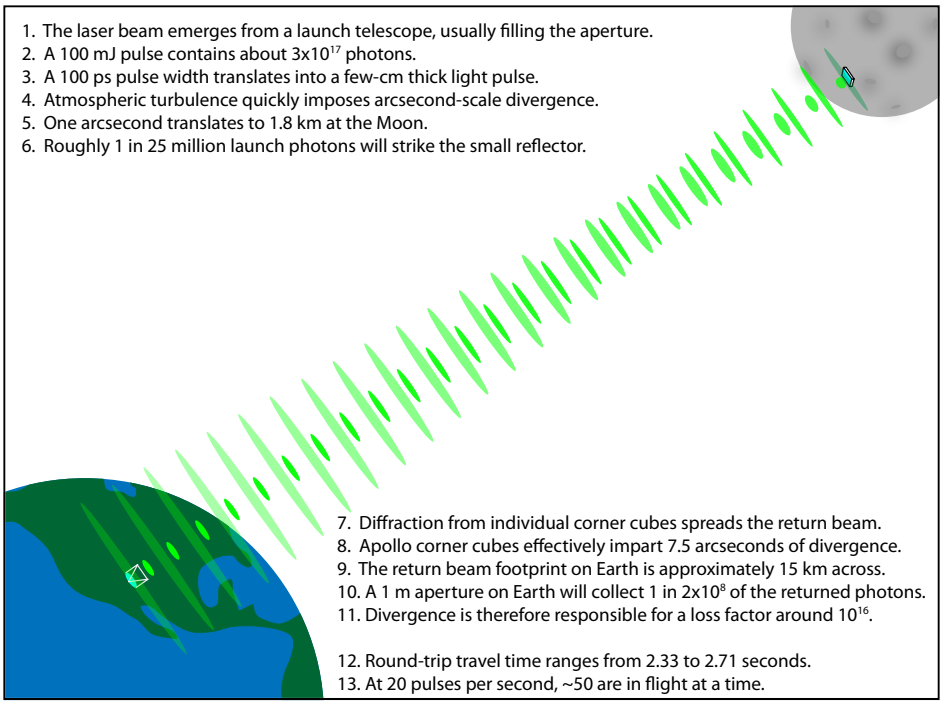

Figure 1-3: Depiction and description of the path of lunar photons as they travel to the Moon and back. Figure from [1].

intercepted light, known as the fiducial signal and used to determine the start time of the lunar laser range, travels through the same optical instruments as the lunar signal, and is further attenuated to match the intensity of the lunar signal (on the order of a single photon per pulse) [13]. APOLLO's detector, consisting of a 4x4 avalanche photodiode array (APD), is sensitive to a single photon [13]. While the APOLLO laser sends out around 3×10^{17} photons per pulse, the divergence due to the earth's atmosphere and the diffraction of the corner cubes on the lunar retroreflector arrays mean that APOLLO sees a return of only about one photon per pulse, or shot. The path the light travels is explained in greater detail in Figure 1-3.

The photon return rate varies depending on the lunar reflector array used, ranging from the record-breaking rates of 0.26 photons/shot for the Lunokhod 2 array to 3.15 photons/shot for the Apollo 15 array [1]. While these rates may seem incredibly low when considering the loss of photons due to divergence, they improve on return rates from other LLR operations by orders of magnitude, namely OCA and MLRS, who regularly saw 0.01 and 0.002 photons/shot rates respectively [1]. While higher

photon return rates do not themselves contribute to better precision, they do allow APOLLO to collect more data more quickly (a higher N, or number of return photons detected), allowing for greater levels of precision due to a larger number of LLR return photons ($\sqrt{N}$ smaller relative to N).

In addition to millimeter precision, APOLLO has also had many other successes. In April 2010, APOLLO rediscovered the Lunokhod 1 rover, which had been lost since the 1970s. Due to its location farther away from the apparent lunar center than the other four retroreflectors, Lunokhod 1 is more sensitive to the orientation and libration of the Moon, making its recovery particularly important and useful. It has also consistently provided better photon return rates than the Lunokhod 2 array since its rediscovery [1]. Additionally, APOLLO is unique among LLR operations in that it is able to collect data during the full moon. Previously, lunar light overwhelmed the returning laser signal, and the direct light on the corner cube retroreflectors caused increased diffraction [14, 15]. Full moon ranging capabilities are important for testing the Equivalence Principle (EP), since violations would be at a maximum along the Earth-Sun line, or at both new and full moons [14]. However, due to the telescope's sun avoidance protocol, ranging is not possible during the new moon, making the full moon the best opportunity to observe any EP violation [12].

1.4 Scope of my work

While APOLLO has made great leaps in terms of precision, the accuracy of the LLR data is not as well known. It is particularly difficult because the data is used to test different gravitational models, but the models themselves are not accurate enough to compare to. Instead, APOLLO has created an internal accuracy test known as the Absolute Calibration System (ACS). In addition to the photons from the lunar signal, the APOLLO detector also receives photons from the ACS in precisely and accurately timed intervals to serve as an accuracy cross-check for the lunar signal. These intervals are determined by a cesium atomic clock connected to a calibration laser capable of sending small pulses at a frequency of 80 Hz, or every 12.5 ns. This

all occurs at a much higher precision than that of the LLR data. The ACS thus superimposes a comb of accurate, known intervals over the fiducial and lunar signals in the data, which allows APOLLO's team to test for potential systematic error and double-check the measurement of Earth-Moon travel time, as well as providing a reference for an independent time source by which to analyze the data [5]. My work with APOLLO centered around making improvements to the existing Laser Slicer Board (LSB), an element of the ACS that acts as a very fast ON/OFF gate for light from the calibration laser, so that the calibration laser pulses only reach the detector when there are also fiducial or lunar signal pulses. In preparation for my work on the Laser Slicer Board (LSB), I developed a more straightforward board, the optoisolator and tiltmeter (opto-tilt) board, which combines optoisolation to eliminate noise from the motor input, logic tests of the optoisolated signals, and a tiltmeter breakout board to act as a local measurement of the telescope orientation. All the electronics design work done on the LSB and opto-tilt board used gschem (for schematic capture) and pcb-rnd (for PCB layout), two open-source versions of electronic design automation software available through the gEDA project.

Chapter 2

Optoisolator and Tiltmeter Board

In this chapter, I will discuss the first circuit board I made for APOLLO, the Optoisolation and Tiltmeter board (opto-tilt board). While the board allowed me to familiarize myself with electrical design and the gEDA software, gschem and pcb-rnd in preparation for my work on the LSB, it also replaced a larger tiltmeter box as well as an opto-isolation board previously installed at APOLLO that was not electrically performing. Due to advances in technology, the opto-tilt board was able to combine these two functions and conserve space on the back of the telescope. The purpose of opto-tilt board is then threefold. First, the board opto-isolates digital signals from the motor, T/R I/O, ACM I/O DSTEP, and the Diffuser Encoder Index. The opto-isolator also functions as a NOT gate, and the opto-isolated signals are then sent through two additional logic gates. Simultaneously, a tiltmeter breakout board measures the orientation of the telescope with the option of choosing the axis of orientation using a jumper. We installed the board on the 3.5 m telescope at Apache Point Observatory in January 2017.

2.1 Optoisolation

The opto-tilt board employs five H11L1 Fairchild Semiconductor 6-pin Schmitt Trigger optocoupler chips to optoisolate the incoming signals. As displayed in Figure 2-1(a), opto-isolation uses light to isolate two electrical circuits. On the input side

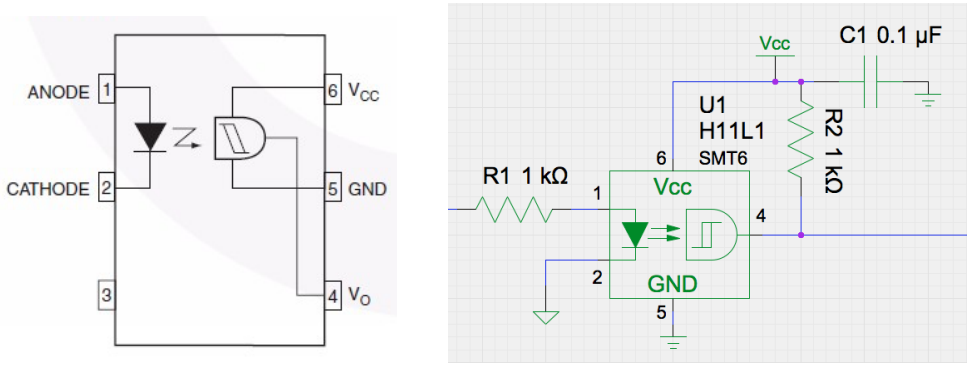

(a) Schematic of H11L1 opto-isolator. Figure from [16].

(b) Schematic of opto-isolation in opto-tilt board.

Figure 2-1: H11L1 optocoupler schematic and implementation in opto-tilt board.

Input	Output
0	1
1	0

Table 2.1: H11L1 Fairchild Semiconductor optocoupler truth table

is a light emitting diode, which is a gallium-arsenide infrared emitting diode in the case of the H11L1 chip used in this board. The output consists of a detector circuit that utilizes a Schmitt trigger for noise reduction. Assuming a quantum efficiency of 100 %, for every electron that goes through the LED, a photon is emitted and then received by the detector, causing an electron to become free and a current to flow. Thus the current is able to be optically transmitted from one ground plane to another, preserving the signal while separating a noisy ground plane from a "clean" one.

Figure 2-1(b) shows the implementation of the Fairchild H11L1 optocouplers in the opto-tilt board. R2 functions as a pull-up resistor between the opto-isolator output and the 5 VDC voltage source. The addition of the capacitor acts as an RC filter to eliminate high-frequency noise. The opto-isolation causes an inversion in logic from input to output, the signal going from high to low and vice versa, as shown in Table 2.1, the optocoupler's truth table. This change is rectified by two logic gates discussed in Section 2.2.

TRSig1	TRSig2	Opto-isolated TRSig1	Opto-isolated TRSig2	XOR
0	0	1	1	0
1	0	0	1	1
0	1	1	0	1
1	1	0	0	0

Table 2.2: Logic Table for Signals from TR1 and TR2 through Opto-tilt Board

TRSig3, DSTEP, DIFF	Optoisolation	NAND as NOT
0	1	0
1	0	1

Table 2.3: Logic Table for Signals from TR3, DSTEP, and Diffuser Encoder Index through Opto-tilt Board

2.2 Logic

The opto-tilt board utilizes XOR and NAND logic chips to perform logic operations and regain the signal from before the opto-isolation. The XOR and NAND chips are both 4-channel and manufactured by Texas Instruments with manufacturer numbers CD74HC86M96 and SN74LS00NSR respectively. Figure 2-6 at the end of this chapter shows the schematic of the most recent revision of the opto-tilt board. The left hand side of the schematic is devoted to the opto-isolation and logic gates discussed in this section.

Table 2.2 traces the path of signals 1 and 2 from the motor rotating the T/R Optic (TRSig1 and TRSig2). After opto-isolation, their logic levels are inverted, and then their signals pass through an XOR gate, which outputs high if they are different and low if they are the same.

Table 2.3 traces the path of all other input signals on the board, or the third signal from the T/R Optic motor (TRSig3), the DSTEP, and Diffuser Encoder Index signals. After the signals are negated by the opto-isolators, they go through a NAND gate used as NOT to regain a now opto-isolated version of the original input signals.

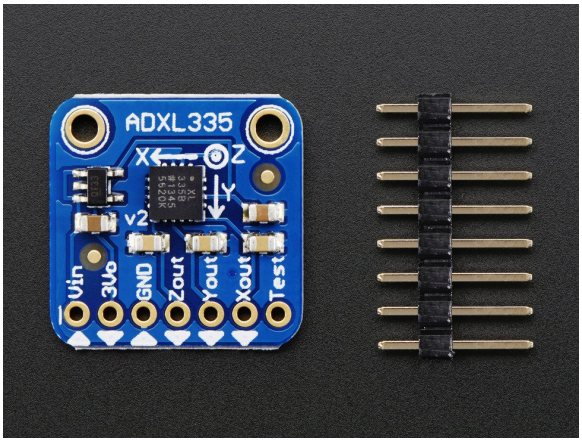

Figure 2-2: Adafruit ADXL335 Accelerometer Breakout Board. Figure from [3].

2.3 Tiltmeter and Calibration

Due to its location on the back of the telescope at Apache Point, the opto-tilt board is a convenient location to include a small breakout tiltmeter to measure the orientation of the telescope. The tiltmeter is powered by the 5 VDC power supply for the optoisolation, and due to this is not completely isolated from the rest of the board, but connected to the "clean" side of the optoisolation. We used an Adafruit ADXL335 triple-axis accelerometer breakout board as our tiltmeter, and the breakout board employs an Analog Systems low power, 3-Axis ±3 g accelerometer (part number: ADXL335). The accelerometer chip can measure both static acceleration, like that of gravity in the tilt-sensing application at APOLLO, or dynamic acceleration [3]. The sensor in the chip consists of a polysilicon structure suspended over a silicon chip. Deflections of a moving mass in this structure due to acceleration destabilize a differential capacitor, which produces a sensor output proportional to acceleration [3]. As the resulting output voltage is also proportional to acceleration, we expect it to vary sinusoidally as the angle of orientation of the telescope changes. Based on the way the opto-tilt board is installed on the telescope, there is a maximum voltage when the telescope approaches 90° (telescope faces zenith) and a minimum voltage when the telescope approaches 0° (telescope faces horizon).

During our on-site installation of the opto-tilt board in January 2017, we took measurements of the output voltage with respect to the orientation of the telescope

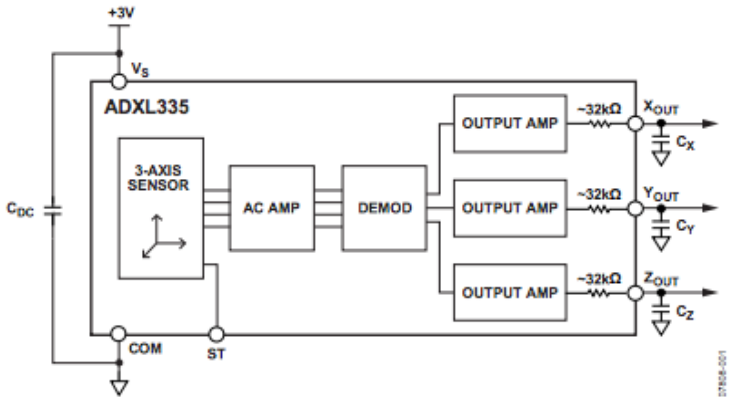

Figure 2-3: Block Diagram of Tiltmeter Breakout Board. Figure from [3].

to determine a calibration fit between angle and voltage. This allows the mission control computer, Houston, to internally determine the orientation of the telescope during runs and provide that information along with the run data. Since the telescope is externally controlled, orientation data would not otherwise be marked alongside other APOLLO data. The 0.045 V voltage difference between the voltage Houston reads and the output voltage from the tiltmeter read on a multimeter was taken into account when determining the fit.

We measured the output voltage from the tiltmeter and from Houston as the telescope was moved in roughly ten degree increments. I then applied a Least-Squares fit to the model $V_{tiltmeter} = A + B\cos(\theta)$ to relate the telescope angle to the output voltage read by Houston. Since Houston uses the voltage from the tiltmeter to determine the angle, I calculated the inverse of the Least-Squares fit model to find the following calibration formula:

$$\theta(V) = \frac{180}{\pi} \arccos\left(\frac{V_{tiltmeter} - A}{B}\right) \tag{2.1}$$

or, with the Least-Squares parameters implemented,

$$\theta(V) = \frac{180}{\pi} \arccos\left(\frac{V_{tiltmeter} - 1.57876619}{-0.32716249}\right) \tag{2.2}$$

where θ is the orientation of the telescope in degrees with 90° corresponding to the

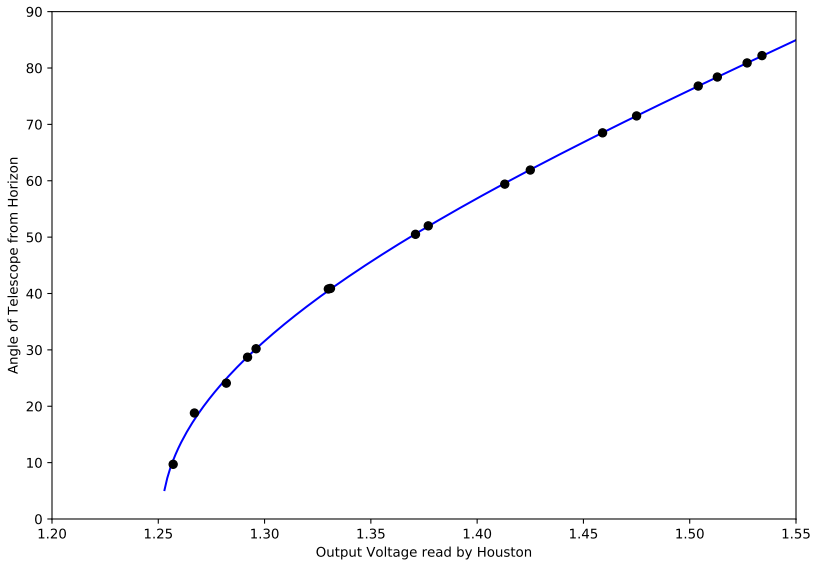

Figure 2-4: Calibration of telescope angle (measured from horizon) as a function of tiltmeter voltage.

telescope pointing towards the zenith and 0° to the horizon. Since the angle range is limited from 0° to 90°, the output voltage of the tiltmeter is constrained to the range $1.2516037093 < V_{tiltmeter} < 1.90592868012$. The plot of this fit over the data is shown in Figure 2-4.

2.4 Summary

As preparation for my work on the ACS Laser Slicer Board (LSB), I developed the opto-tilt board to replace a large tiltmeter box and an opto-isolation board that was not electrically functioning. After I populated, tested and installed the opto-tilt board, it is now part of routine operation at APOLLO. I also calibrated the voltage of the tiltmeter breakout board as a function of angle for APOLLO's system, thus determining a relationship between the two, which Houston, the system's computer, uses for data processing and logging.

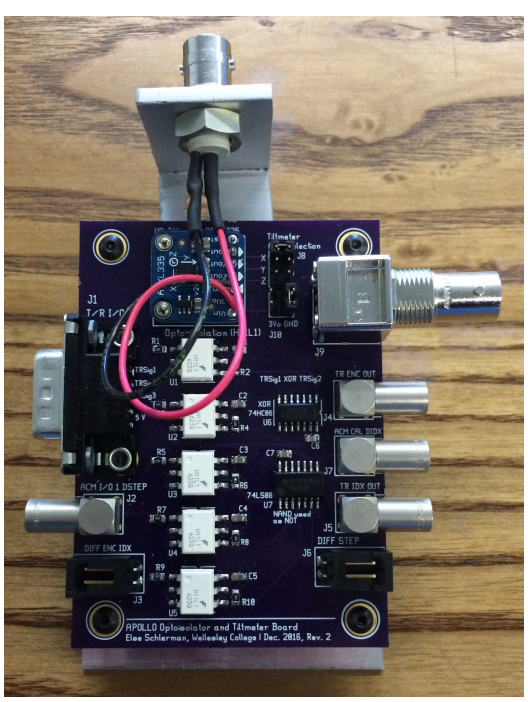

(a) Populated opto-tilt board at Apache Point Observatory before installation.

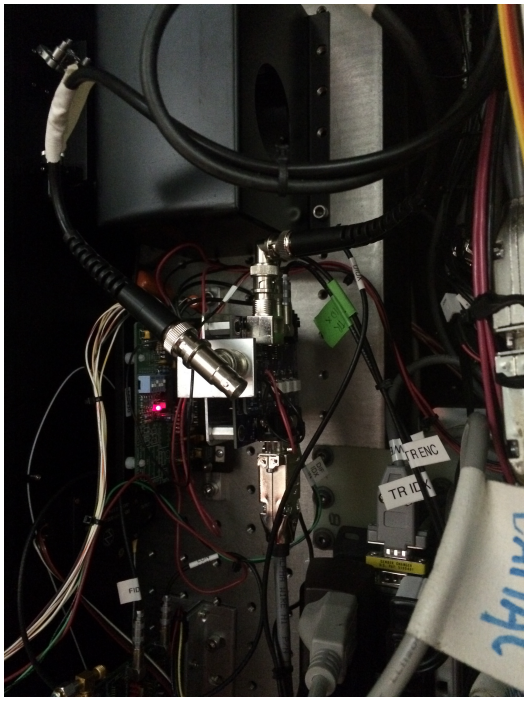

(b) Installation of opto-tilt board on 3.5 m telescope at Apache Point Observatory.

Figure 2-5: Photos of opto-tilt board before and after installation.

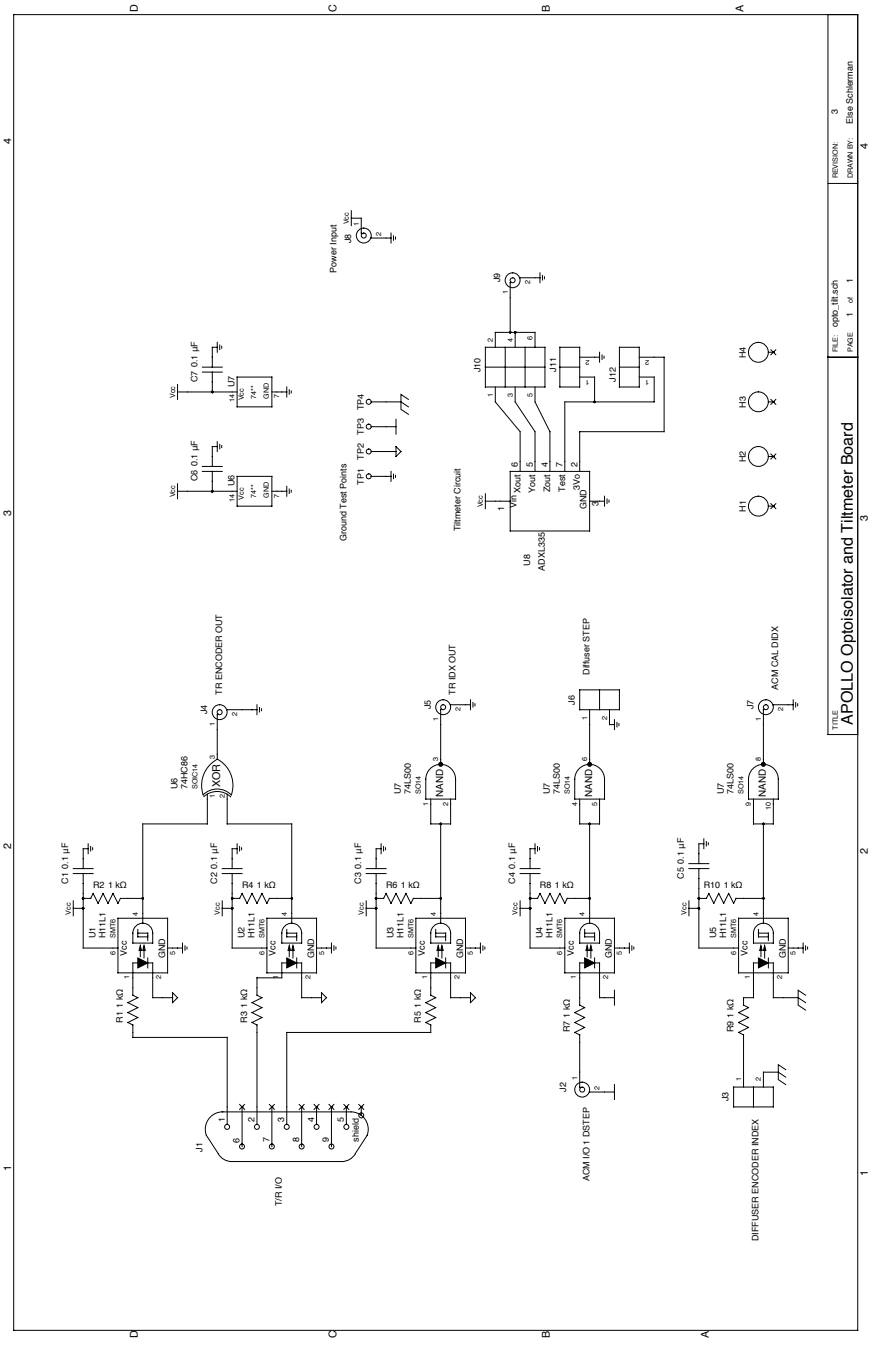

Figure 2-6: Schematic of third revision of opto-tilt board.

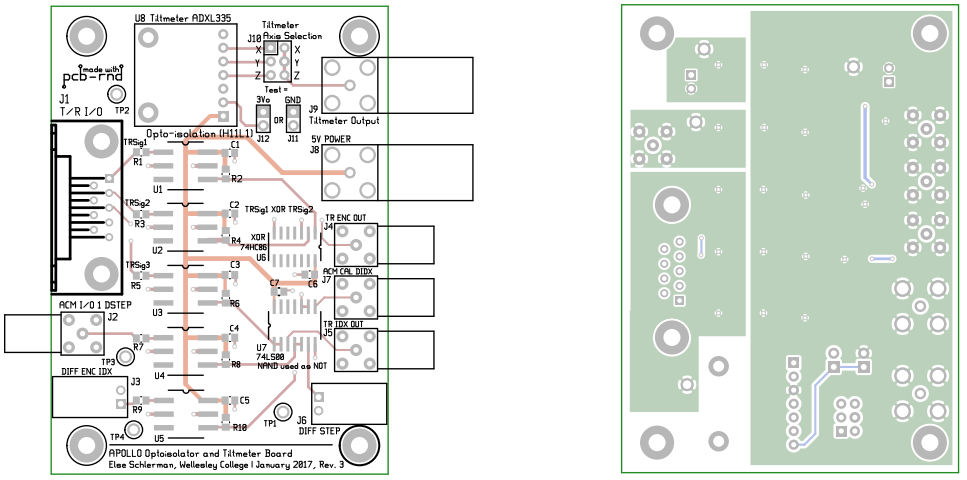

(a) PCB layout of top layer of opto-tilt board.

(b) PCB layout of ground/bottom layer of opto-tilt board.

Figure 2-7: PCB layout of top and bottom of 2-layer opto-tilt board. Looking from left to right on the top layer of the PCB, the board consists of input connectors, opto-isolators, logic gate chips, and output connectors. The tiltmeter breakout board and power supply occupy the top region of the board. In the ground layer of the board, the separation of four ground planes is clearly demarcated, with the opto-isolation occuring across the central vertical divide. On the left are the separated ground planes of the various motor inputs, while the large ground plane on the right side is connected to the clean opto-isolated signals.

Chapter 3

Absolute Calibration System

A separate manuscript on the APOLLO Absolute Calibration System entitled *Achieving millimeter precision in lunar laser ranging* is in preparation for submission to *Classical and Quantum Gravity*, of which I am a co-author. In the following author list, underlined names represent Wellesley undergraduates: T. Murphy, Jr., J.B.R. Battat, N. Colmenares, E. Adelberger, C.D. Hoyle, L. Huang Ruixue, E. Schlerman, C. W. Stubbs.

The Absolute Calibration System (ACS) acts as an internal, precise, and accurate reference for APOLLO's time measurements. A high frequency laser sends short pulses of light to the APOLLO detector to overlay a comb of well-known time points over lunar and fiducial return signals. In this way, the ACS laser acts as an optical clock by which to accurately compare APOLLO's time measurements.

3.1 Motivations behind ACS

While APOLLO has consistently achieved precision on the millimeter range ($\sim$2 mm) in the past years, until recently the accuracy of the measurements was not known. Similar to the traditional bullseye diagram, like the one shown in Figure 3-1, the addition of the ACS allows the accuracy of APOLLO measurements to match their precision. The motivation for creating an internal accuracy check as opposed to a model-based one comes from the complexities of the gravitational models that LLR

data tests. Comparison between APOLLO data and the best solar system models gives residuals on the order of a centimeter (∼15 mm for the best models, but even higher for others), an order of magnitude larger than the precision of data. Because of this discrepency between ranging data and model, before the ACS, it was uncertain if the model itself was incomplete or rather if the ranging data were not as accurate as precise. In addition, while LLR has seen great improvements in the precision of measurements in the past thirty years, the scale of these improvements has not been matched in tests of gravity and the scientific deliverables. This is greatly due to the intricacy of the system being modeled, and all the physical factors playing into a measurement of a photon traveling from the surface of the Earth to the Moon and back.

Because of the question arising from the large model residuals – whether this is due to an error in the model or in the data – it became apparent that a method of testing data accuracy independent of the models was necessary to improve understanding of the system. The Absolute Calibration System employs a high-frequency laser fixed at an 80 MHz frequency given by a cesium clock, and users are able to remotely select sections of the calibration laser pulse to be delivered to the APOLLO system detector, the avalanche photodiode (APD) array detector. The cesium clock has a stability, $\Delta f/f$, of $\sim 10^{-13}$, which corresponds to < 1 ps of the ∼2.5 s roundtrip time of a photon travelling to the moon and back. In comparison, APOLLO's millimeter precision corresponds to about 7 ps of the one-way path. The laser pulses then have less uncertainty than APOLLO's time measurements, and provide a both accurate and precise time cross-check for ranging data. This system allows APOLLO users to better explore the accuracy of the LLR data measurements as well as investigate possible sources of systematic error.

3.2 ACS System Overview

Driven by a cesium atomic clock, a high-frequency laser sends short pulses of light at 80 MHz to the 16-element APD array on top of lunar and fiducial return signals.

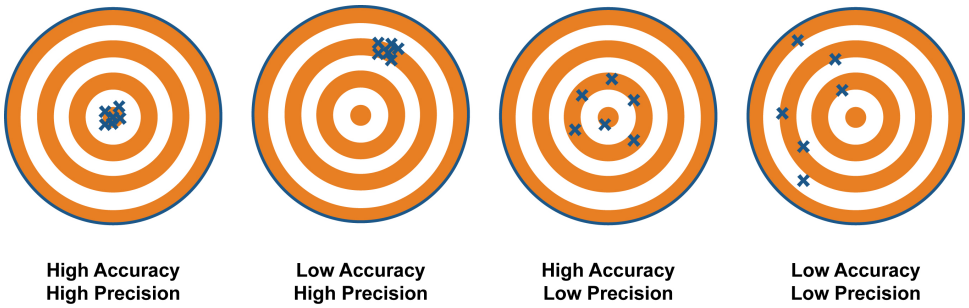

Figure 3-1: Visual depiction of accuracy versus precision. Figure from [4].

An 80 MHz cesium atomic clock (5071A) drives the calibration system and provides a clock reference separate from APOLLO's XL-DC 50 MHz GPS-disciplined clock. The dominant purpose of the cesium clock is to act as the frequency reference for a high-repetition-rate PicoFYb laser, which generates a constant stream of pulses of light at 80 MHz. These pulses are in the infrared range with a wavelength of 1064 nm [5]. The second function of the cesium clock is to provide a frequency comparison to the GPS-disciplined clock in the Universal Counter located in the ACS box. By comparing the two clocks (as discussed in Chapter 4), one can monitor the drift of the GPS-disciplined clock relative to the cesium clock [5].

The ACS is physically divided into two different boxes, the ACS Box and the Utah Box, the contents of which are shown in Figures 3-2 and 3-3 respectively. The ACS box is located on the intermediate level of the telescope and is temperature controlled, while the Utah Box rides along with the telescope [5]. The ACS box is connected to the Utah Box by a 12.2 m fiberoptic cable which transmits the IR pulse from the PicoFYb laser in the ACS box. The reason for the isolation of the ACS box from the Utah Box and telescope is the electromagnetic interference created by the powering of the lunar laser. Switching on the lunar laser involves powering it to ∼3000 V in a few nanoseconds, and the resulting electromagnetic interference has the potential to affect the electronics in the vicinity used for timing and detecting [17].

Figures 3-3 and 3-4 show the path of the IR laser light from the ACS laser as it transforms into the appropriate form of an "optical ruler" and is then sent to the APD. While the laser output is a constant stream of IR light pulses at 80 MHz, it

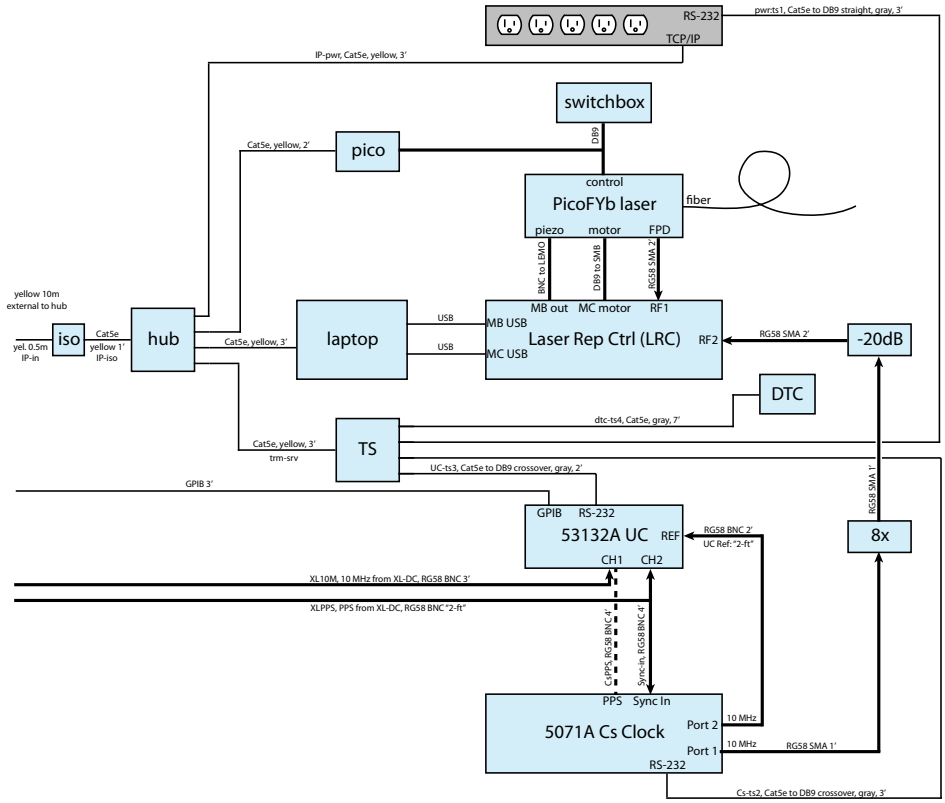

Figure 3-2: Components in the ACS Box. Figure from [5].

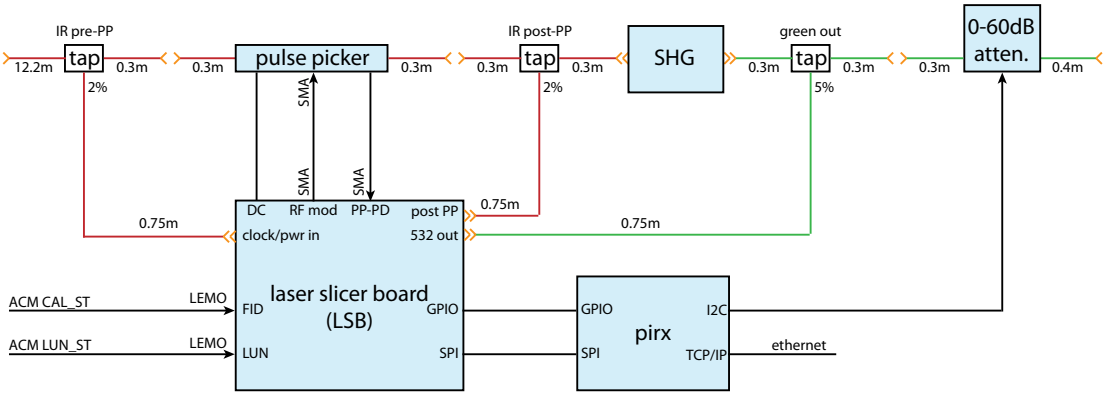

Figure 3-3: Components in the ACS's Utah box. Figure from [5].

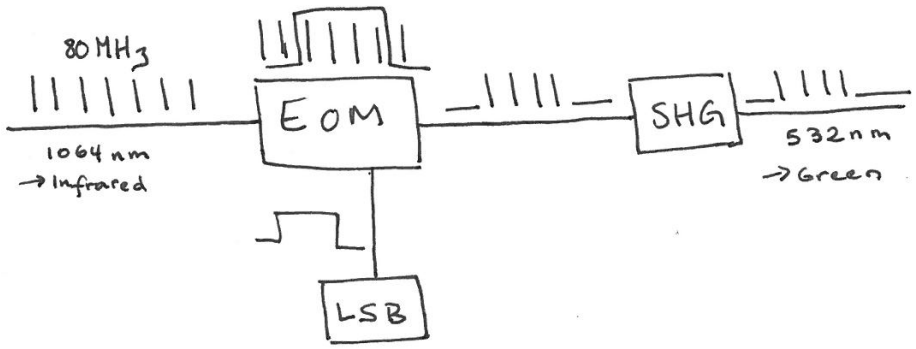

Figure 3-4: Depiction of laser pulses through ACS.

is only necessary to have the calibration laser pulses reach the detector when there is also a return signal from either the fiducial corner cube or a lunar pulse. Timing electronics count the number of pulses between the fiducial and lunar signal that are not seen on the detector, so as to be able to determine the round trip travel time of a photon. The ACS employs an electro-optic modulator (EOM) to select only a certain set of calibration laser pulses to send to the detector (corresponding to lunar and fiducial signals). The Laser Slicer Board (LSB) determines the "gate" for which the EOM, or "pulse picker," passes the calibration laser pulses based on lunar and fiducial alert signals. After traveling through the pulse picker, the small selection of laser pulses that are transmitted are then sent through a second-harmonic generator (SHG), which halves the wavelength of the laser light to 532 nm, green in the visible light range. That signal is further attenuated and then sent to the detector.

The reason behind this order of operations – pulse picking first and generation of green laser light second – comes from limitations of the parts used in the system. It is important to have green photons of wavelength 532 nm reach the detector as the end result because those are the same photons produced by the APOLLO lunar laser for Earth-Moon distance measurements. However, pulse pickers perform better in the infrared, and the laser company manufactures a series of fiber lasers of various wavelengths in the infrared. For the fiber lasers like the one APOLLO uses for the ACS calibration laser, the doping of the fiber determines the wavelength in the infrared

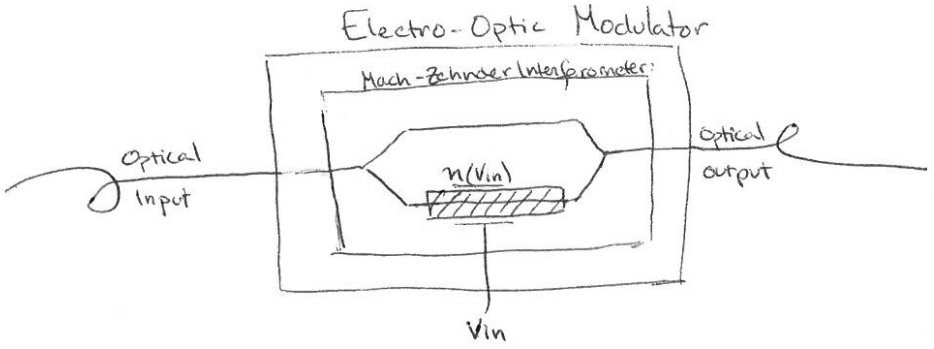

Figure 3-5: Cartoon of Electro-Optic Modulator.

range. Then, it was simply necessary to find a fiber laser with a wavelength of 1064 nm, so that the wavelength could be halved by a SHG.

The EOM employs a Mach-Zehnder Interferometer that has a voltage-controlled phase shift, and is depicted in Figure 3-5. The light entering the EOM splits equally into two paths. One of these paths travels through a crystal that has an index of refraction dependent on an applied voltage, or $n(V)$. Since the speed of light through a material is given by $v = c/n$, changing n allows us to vary the speed of the light traveling through the crystal path of the EOM relative to the light traveling through the other path. When the two beams are recombined, depending on the relative phase difference between the two, they will either be completely in phase, out of phase, or somewhere in between. V_π is defined as the voltage that causes the change in n equivalent to the transition from completely destructive interference to completely constructive interference, or vice versa. As its name suggests, V_π is the voltage corresponding to a shift of π in the phase, or electronically a shift from full suppression to full transmission of the light [5]. Most of the time, the EOM is out of phase and no light is transmitted, but when requested the LSB produces a voltage pulse of V_π and an appropriate width, which triggers a gate for the EOM to pass calibration laser light to the APD.

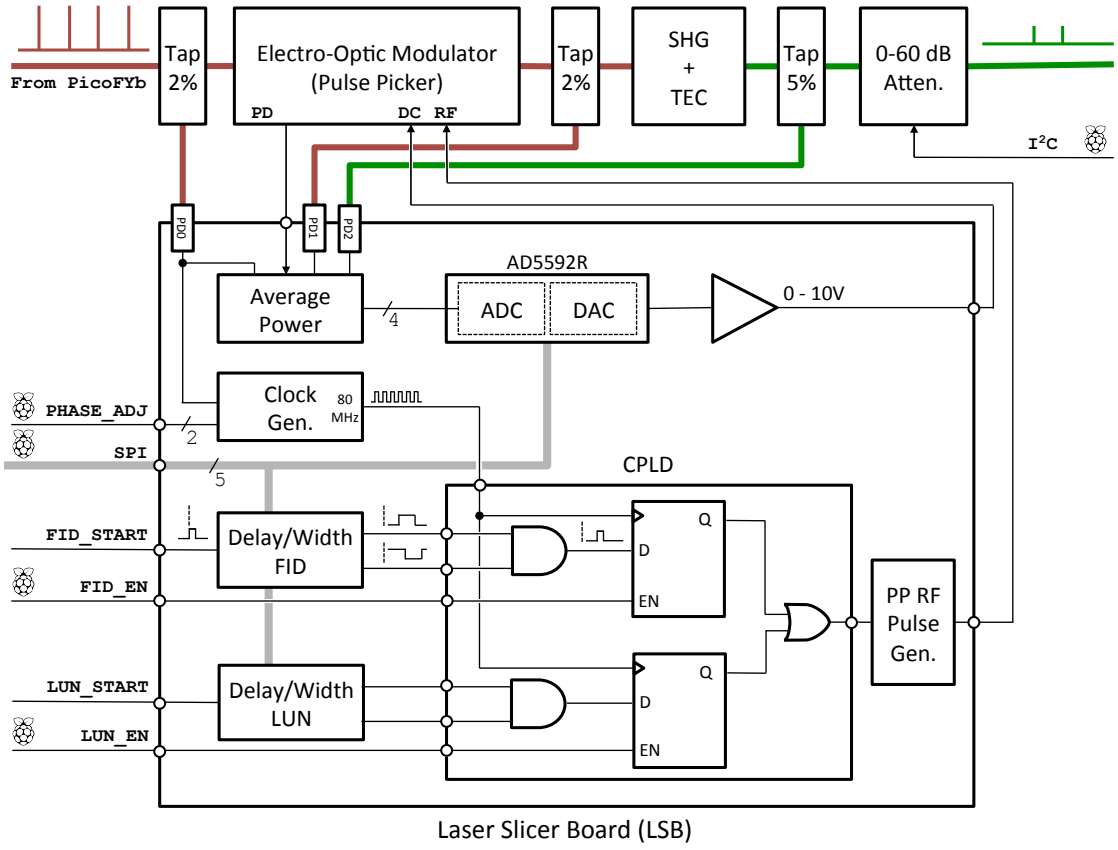

Figure 3-6: Block diagram of components in the Utah box and of the LSB.

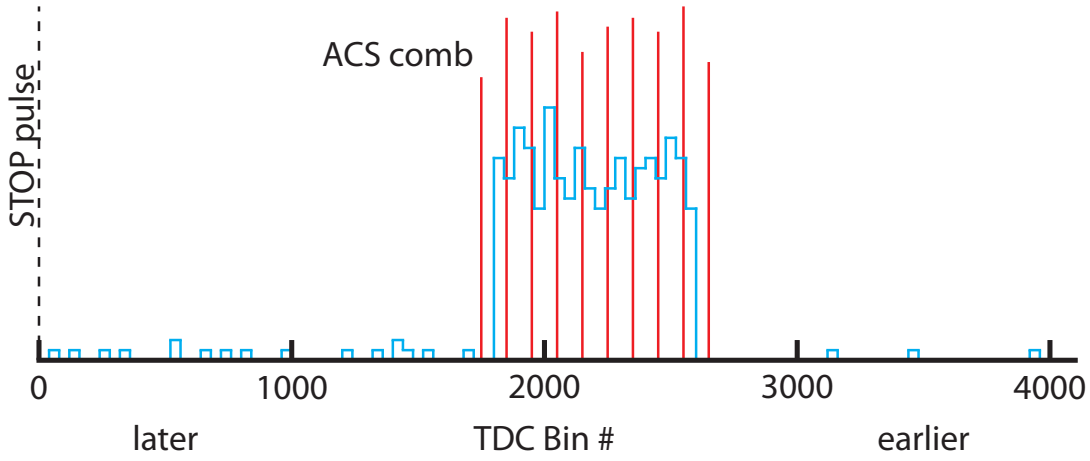

Figure 3-7: Depiction of ACS calibration laser pulses superimposed on an APOLLO signal. The ACS photons, or the "teeth" of the comb, appear every 2.5 ns. While signal photons, arriving randomly relative to the 50 MHz clock, are distributed evenly throughout the 20 ns clock period, ACS photons in sync with the 80 MHz clock arrive at eight distinct positions relative to the period of the 50 MHz clock. Figure from [5].

3.3 Laser Slicer Board

The Laser Slicer Board or LSB is the "brain" of the ACS with the purpose of generating a gate for the electro-optic modulator (EOM), or pulse picker, based off of given lunar or fidicial input signals. Three main parts of the board, Clock Generation, Delay/Width Generation and CPLD, and Average Power, all depicted in Figure 3-6, allow for the LSB to do this task as well as for APOLLO to remotely determine that the ACS is functioning as expected. The task of generating a gate for the EOM is non-trivial with respect to timing because the square-wave pulse gate must have rising and falling edges lying in between the delta pulses of light coming from the calibration laser. Since the laser is pulsing at 80 MHz, it means that there is a time window of 12.5 ns in which to have the rising edge. The Clock Generation creates an electrical clock signal in time with the 80 MHz cesium clock, which is used to calibrate the delay time between the lunar or fiducial alert and the gate generation. Fine phase adjustment in the clock generation part of the board allows APOLLO to adjust the delay of the gate so that the rising and falling edges come between calibration laser pulses. The Delay/Width Generation part of the board together with

the CPLD change the delay and width of the lunar or fiducial alert signal to form the gate pulse to user-determined specificaitons. Generally, these specificaitons are designed so that the optical ruler from the ACS falls on the lunar or fidicual signal at the APD, as depicted in Figure 3-7. The delay and width of the gate are also set in multiples of the period of the 80 MHz clock. Finally, the LSB takes average power measurements of the 1064 nm IR light before and after the EOM, the green 532 nm light after the SHG, and the light of the unchanged path of the Mach-Zehnder interferometer, converts these measurements from analog to digital, and sends these to the system's control computer, a Raspberry Pi named `pirx`. These average power measurements are then recorded and used as a reference to make sure that the system is behaving normally.

Complete LSB schematics are located in Appendix A.

3.3.1 Clock Generation

The purpose of the clock generation section of the LSB is to convert the delta pulses coming in at 80 MHz from the IR photodiode into an 80 MHz square wave pulse clock with a 50% duty cycle. This is achieved through four steps and four corresponding chips:

1. Convert analog signal to logic pulse.
2. Convert digital signal to have 50% duty cycle.
3. Convert LVPECL signal to LVTTL.
4. Convert frequency back to 80 MHz and allow for remotely requested phase shift.

These four steps are depicted in Figure 3-8.

To perform the first step, APOLLO uses a single-supply, high speed comparator from Analog Devices (manufacturer number: ADCMP553BRMZ). The comparator takes in the output from the photodiode, which converts the 80 MHz IR pre-pulse picker laser light from the 12.2 m fiberoptic cable into delta pulses of current at 80 MHz. The comparator then converts these analog pulses into a digital LVPECL

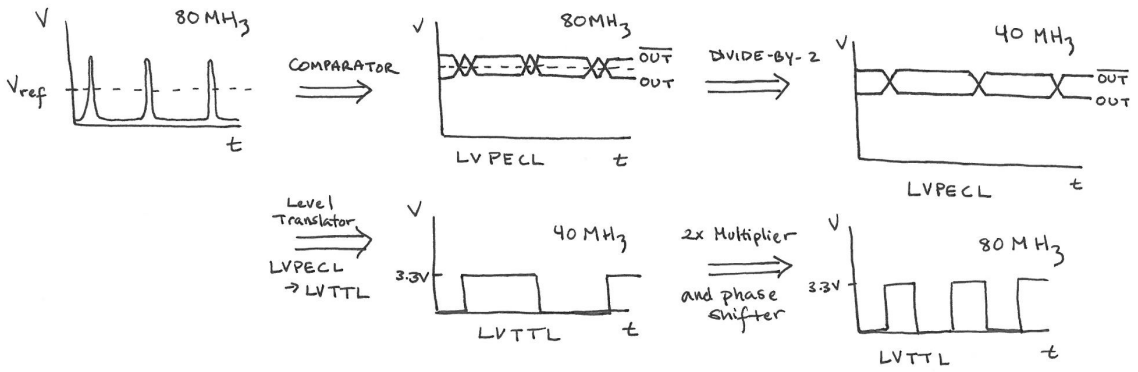

Figure 3-8: Depiction of current and voltage at various steps throughout clock generation in LSB.

signal, and its complement. The output voltage is high when there is a current pulse and low otherwise, based off of a given reference voltage. The complement of the output is then the inverse of this. This system is immune to common mode noise because only the differential signal matters in the logic pulse. One can ignore the addition of any DC voltage offset, because the absolute signal of either the output or its complement is unimportant.

The output and complement of the output of the comparator then go into the differential clock inputs for the 3.3 V ECL 2 Divider chip manufactured by ON Semiconductor (part number: MC100LVEL32DG). This chip changes the logic of its output for every input rising edge. This means that when there is a high pulse from the output of the comparator (or a rising edge), the output from divider will be high until the next high pulse from the comparator, at which it will change to low. This creates a 50% duty cycle, but the frequency is halved. The output is then a 40 MHz LVPECL differential signal.

The next chip, an ON Semiconductor 3.3 V Dual Differential LVPECL to LVTTL Translator (part number: MC100EPT23DG), converts the differential LVPECL logic signal to an absolute LVTTL logic signal. While the output signal is now the proper form for the clock – 50% duty cycle and TTL logic – the frequency is 40 MHz, half of the desired clock frequency.

The final step in the clock generation is to then multiply the frequency of the signal by two and allow for delay adjustment. Both are done through a powerful Texas Instruments Clock Multiplier with Delay Control and Phase Alignment chip (part number: CDCF5801ADBQR). This chip multiplies the frequency by 2, giving an 80 MHz clock output (with a period of 12.5 ns). It allows for fine adjustments of the clock's phase on the order of one period with the resolution of 0.234° per step (or 1536 steps per 360° of phase) giving the ACS the ability to shift the EOM gate relative to laser pulses. This signal provides the clock reference for the CPLD.

3.3.2 Delay Generation and CPLD

The delay generation section of the LSB adjusts the width and delay of the ACS gate so that the gate is aligned with the fiducial or lunar return signal. Delay generation is triggered by a signal from APOLLO, as either a fiducial or lunar alert, which means that APOLLO has requested a laser fire. This comes in the form of a 20 ns pulse – 20 ns being the period of APOLLO's 50 MHz system clock. Figure 3-9 depicts the voltage pulse throughout this process.

The first part of the delay generation process is to broaden the 20 ns pulse using a monostable multivibrator, or "one-shot." APOLLO uses a Nexperia USA Inc. one-shot (part number: 74LVC1G123DP,125). The rising edge of the 20 ns input pulse makes the output go high one time, and the width of the output pulse is set by the values of a resistor and capacitor. The capacitor in APOLLO's circuit is fixed, while the resistor is a potentiometer adjusted to give a 150 ns pulse width.

The signal from the one-shot serves as the input for two identical delay chips, which I will call delay chip 0 and delay chip 1. The delay chips are Dallas Semiconductor 8-Bit Programmable Timing Elements (part number: DS1023S-50+). These delay chips have two different outputs: the output and its complement. APOLLO takes the output of delay chip 0 and the complement of the output from delay chip 1. `pirx` remotely sets the delays of these two chips, Δt_0 and Δt_1 respectively.

The two signals travel into the CPLD, or complex programmable logic device, which takes the AND of the signals, producing a pulse of width $\Delta t_1 - \Delta t_0$ with a

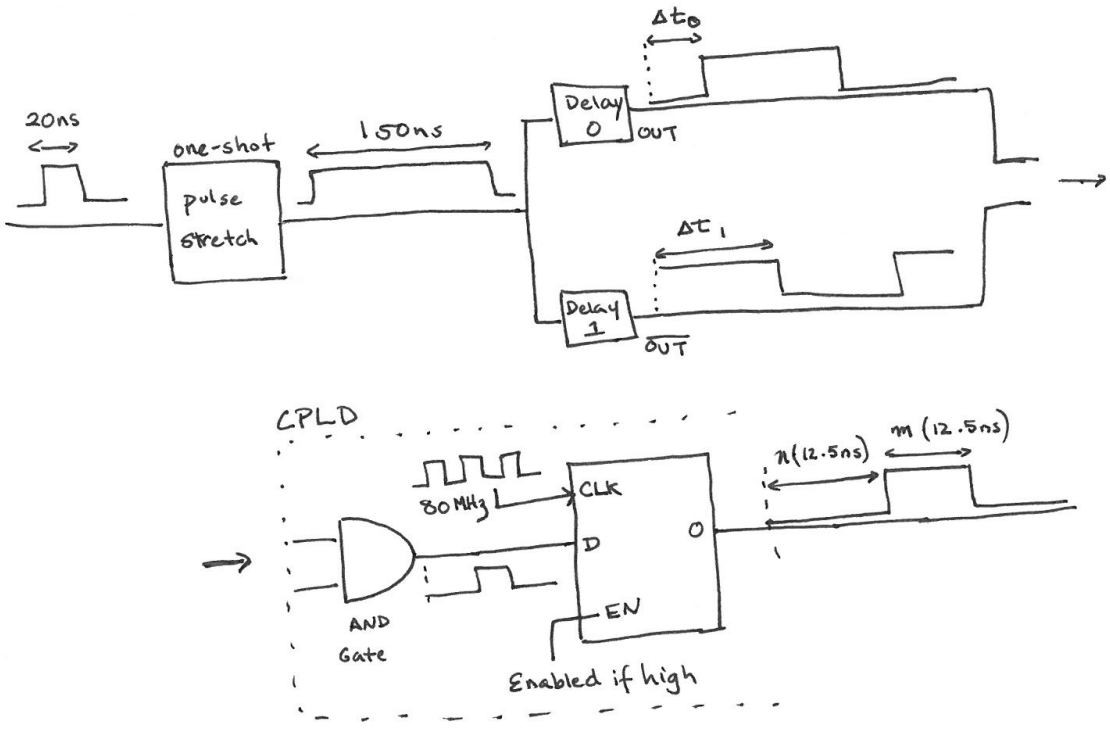

Figure 3-9: Cartoon of pulse throughout delay generation and CPLD in LSB.

delay of Δt_0. The signal from the AND gate then becomes the input for a D-type Flip Flop (DFLOP) inside the CPLD. The DFLOP uses the 80 MHz clock as explained in Subsection 3.3.1 as its clock reference and will only give an output Q if the signal at its EN input is high. The DFLOP functions as depicted in Table 3.1. Q only changes state on a rising edge of CLK. Q is set to the state of the input D at the time of a CLK rising edge. The output follows input for one clock cycle, which synchronizes the delay signal back to the 80 MHz ACS clock, as opposed to the 50 MHz system clock that requests the delay originally. It is pivotal to open the gate on the ACS clock, rather than the APOLLO Command Module (ACM) clock, so that the gate brackets the laser pulse. This gives the delay for the gate in increments of the 80 MHz clock - a "coarse" delay–, and allows the multiplier chip in the clock generation section of the board to fine tune the delay over a period of the 80 MHz clock.

The width of the delay pulse is also then some integer multiple of 12.5 ns, the 80 MHz clock period. The pulse width will be equal to $n * 12.5\,\text{ns}$ where $n = \frac{(\Delta t_1 - \Delta t_0)}{12.5\,\text{ns}}$ rounded down to the lowest integer.

D	CLK	Q
H	↑	H
L	↑	L

Table 3.1: Logic table for delay signal through DFLOP if EN is high.

The output from the DFLOP is either 0 or 5V, and is used to trigger a pulse from a pulse generator which creates the appropriate V_π for the EOM. The current of this signal also needs to be boosted before being sent to the EOM due to the EOM's 50 Ω input impedance.

3.3.3 Average Power Measurement

This section of the board measures the average power of the laser light at four points along the calibration laser's path through the pulse picker and SHG to determine remotely that everything is functioning as expected. Photodiodes located on the LSB convert the IR light pre-pulse picker, the IR light post-pulse picker, the green light post-SHG, and the IR light of the unchanged path of the EOM to electrical signal. Here, the average power measurement refers to the average power of the laser light. APOLLO measures these by converting the light to current that is proportional to the power of the light through a photodiode. The current is then converted to voltage, averaged, and measured. The analog voltage measurements corresponding to average power are converted to a digital signal through an Analog to Digital Converter (ADC) and then sent to `pirx` for logging and processing.

For each average power measurement, the LSB converts the signal from the photodiodes – essentially delta pulses of current in time – into an steady DC voltage corresponding to the average voltage of the pulses. As shown in Figure 3-10, the LSB employs two opamps in series, the first acting both as a current-to-voltage converter and the second as an inverting amplifier. The first op amp converts the delta functions of current in time from the photodiode into a voltage of the opposite sign. The op amp also has an averaging effect due to the frequency dependence of its open loop gain, a phenomenon discussed in Subsection 3.3.4. A second op amp inverts the

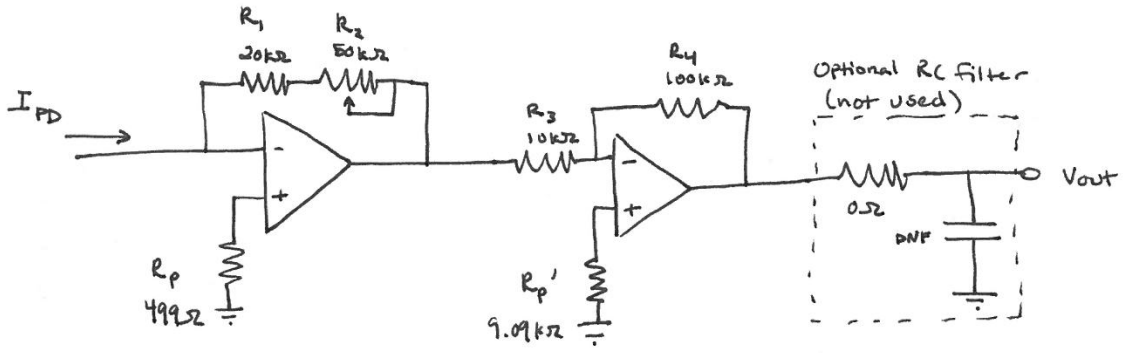

Figure 3-10: Example average power circuit from LSB with resistor values.

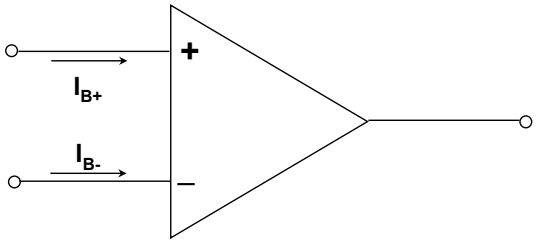

Figure 3-11: Input currents of a non-ideal op amp. Figure from [6].

voltage signal and also amplifies the signal by 10. This gives a positive final voltage, which is necessary since the ADC only takes positive values.

Because we are working with non-ideal op amps, resistors R_P and R'_P in Figure 3-10 are included in the circuit to correct for the effect of the op amp's non-zero input bias current. While ideally no current flows into the inverting and non-inverting terminals of an op amp, there are in fact two small input bias currents, I_{B+} and I_{B-}, as shown in Figure 3-11 [6]. These bias currents can interact with external impedances and produce voltages that are amplified by the system gain. Even with a null offset voltage (an aspect of non-ideal op amps discussed in Subsection 3.4.1), an inverting amplifier circuit will have a non-zero output voltage if $V_+ = 0$, or the non-inverting terminal is grounded, because of the input bias currents' interactions with the resistors in the circuit [7]. The inverting terminal "seeing" the parallel resistance of R_1 and R_2 creates a voltage $V = I_{B-}(R_1 \parallel R_2)$, which is then amplified by the system gain. In order to cancel out this linear addition to the output voltage of the op

amp, one can add an equivalent resistance to the non-inverting input terminal of the op amp. By putting a resistor, R_P, equal to the parallel resistance between V_+ and ground, one can null the voltage created by the bias current from the non-inverting input terminal. These resistors are labeled as R_P and R'_P in Figure 3-10. Note that Figure 3-10 does not show the resistor in parallel with R_1 and R_2 that determines R_P.

3.3.4 Bandwidth of an Op Amp

The Average Power section of the LSB was designed to use the limited bandwidth of an op amp as a means of averaging the high-frequency signal from the calibration laser. In the ideal, we consider the open loop gain, A_{OL}, of an op amp to be infinite for all frequencies, but in practice the gain is finite and rolls off at high frequencies in a fashion similar to a single-pole RC low-pass filter. The gain-bandwidth product (GBP or f_T) is an op amp specification, which gives the frequency at which the gain is unity. Like a single-pole low-pass filter, the op amp open loop gain rolls off at a rate of 6 dB/octave [7].

The Analog Devices op amps (part number: AD824ARZ-14) APOLLO uses in the LSB have a gain-bandwidth product of 2 MHz. When used with frequencies above this specification, the op amp cannot keep up with the rapid changes at the input and acts as an integrator, like the low-pass filter at high frequencies. This flattens the pulse, averaging the voltage of the high frequency signal.

Mathematically, we show this effect by analyzing the frequency dependence of the transimpedance of our circuit, depicted in Figure 3-13. The transimpedance, Z_m, of a current-to-voltage converter is defined as the ratio of the output voltage to input current, or using the names of components as given in Figure 3-13, $Z_M = e_o/I_{PD}$.

Because the op amp open loop gain (A_{OL}) is finite, we can determine the error voltage at the inverting input using the expression:

$$e_o = A_{OL}(e_p - e_m) \tag{3.1}$$

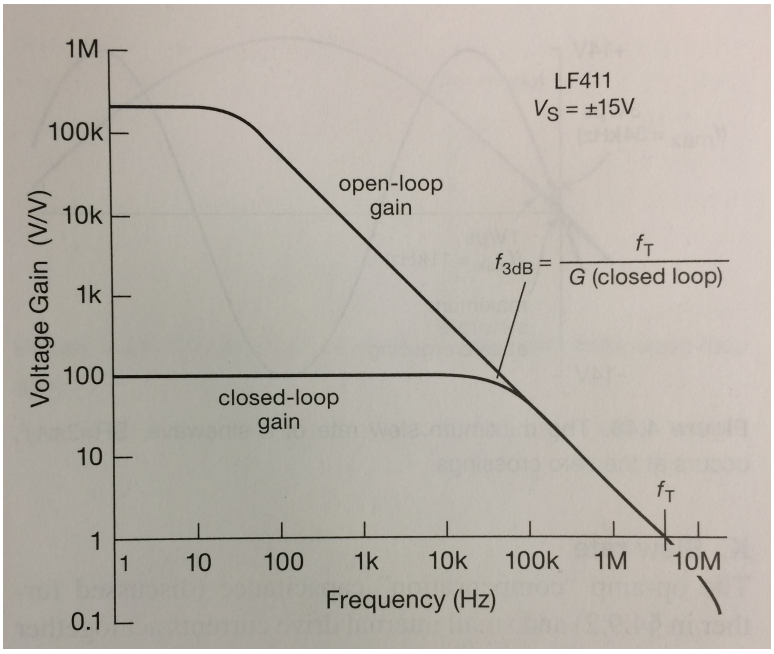

Figure 3-12: Frequency dependence of gain for a LF411 op amp. Figure from [7].

where e_o is the output voltage, e_m is the voltage at the inverting terminal, and e_p is the voltage at the non-inverting terminal. Since the non-inverting terminal is connected directly to ground, $e_p = 0$, and we find

$$e_m = -\frac{e_o}{A_{OL}}. \tag{3.2}$$

Because the current flowing into the inverting terminal is equal to zero due to the second Golden Rule of op amps, using Kirchoff's Current Law at the summing junction allows us to set I_{PD} equal to I_f. Using Ohm's Law, we can determine I_f, and by extension I_{PD}:

$$\begin{aligned} I_f &= \frac{e_o - e_m}{R_f} \\ &= \frac{e_o - (-e_o/A_{OL})}{R_f} \\ I_f &= \frac{e_o(1 + 1/A_{OL})}{R_f} = I_{PD}. \end{aligned} \tag{3.3}$$

We now find an expression for the transimpedance related to the open loop gain,

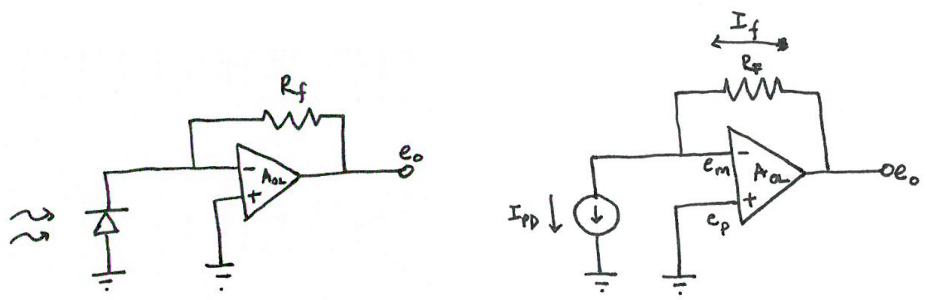

(a) Current-to-voltage converter circuit. (b) Current-to-voltage converter circuit model.

Figure 3-13: Current-to-voltage converter circuit used for transimpedance analysis.

which has a frequency dependence

$$Z_m = \frac{e_o}{I_{PD}} = \frac{R_f}{1 + \frac{1}{A_{OL}}} \tag{3.4}$$

In the range we are considering, where $f \sim f_T$, $|A_{OL}| \propto 1/f$ with $|A_{OL}| = 1$ at $f = f_T$ [7]. More precisely,

$$A_{OL} = \frac{f_T}{jf} = \frac{\omega_T}{s} \tag{3.5}$$

where we define $\omega_T \equiv 2\pi f_T$ and $s \equiv j\omega = j2\pi f$. This gives us an expression of Z_m that is linear in s in the demoninator, or single-pole:

$$Z_m = \frac{R_f}{1 + \frac{s}{\omega_T}}. \tag{3.6}$$

Written in terms of frequency instead of angular frequency, we find the transimpedance of our current-to-voltage converter to be

$$Z_m = \frac{R_f}{1 + j\frac{f}{f_T}}. \tag{3.7}$$

The magnitude of this complex number is given by

$$|Z_m| = \frac{R_f}{\sqrt{1 + (\frac{f}{f_T})^2}}, \tag{3.8}$$

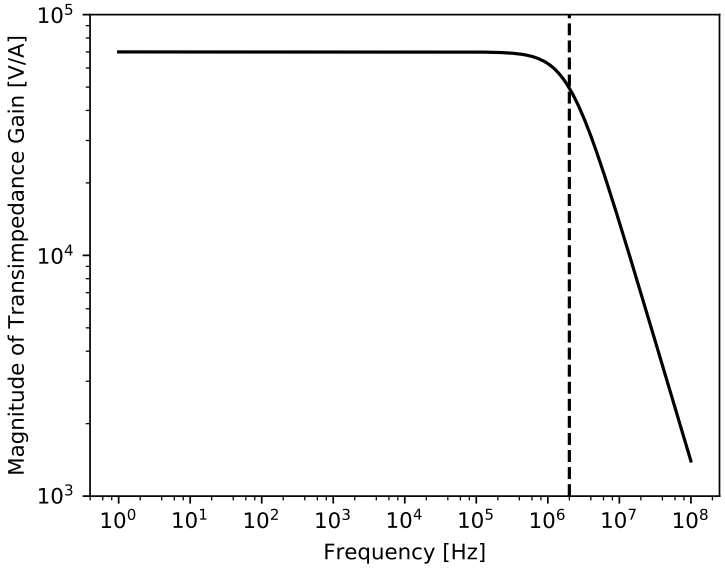

Figure 3-14: Magnitude of transimpedance gain of current-to-voltage converter as a function of frequency. For this plot, $R_f = 70\,\mathrm{k}\Omega$ and $f_T = 2\,\mathrm{MHz}$, and were chosen to match the resistor values and op amp specifications of the components in the LSB. We see that at low frequencies, $|Z_m| = 70\,\mathrm{k}\Omega$, as expected for $f \ll f_T$ in Equation 3.8. The dashed vertical line demarcates the location of f_T.

which is plotted with respect to frequency in Figure 3-14. As we can see in the figure, for frequencies at or above the gain bandwidth product, f_T, the transmission of the op amp has the same dependence on frequency as a single-pole low-pass filter, with increasing attenuation as the frequency increases. Since the pulses reaching the op amp have a frequency of 80 MHz, they fall well within this attenuation range and are suppressed, resulting in an averaged output signal. In this way, we can manipulate the op amp to perform the averaging of the input signal.

3.4 Upgrades to LSB

In this section, I will detail the revisions I made to the LSB as part of my thesis work.

In the first version of the LSB, the photodiode average power measurement was affected by the offset voltage, V_{OS}, of non-ideal op amps, discussed in Subsection 3.4.1. The offset voltage reduced the dynamic range of the system and diluted the ability to measure the correct extinction ratio of the laser light coming out of the EOM. The

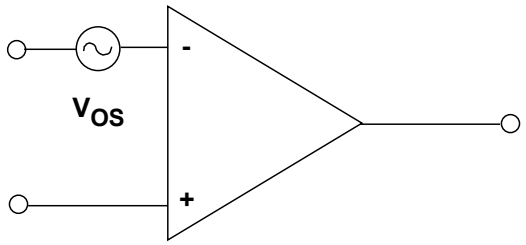

Figure 3-15: Depiction of non-ideal op amp with offset voltage. Figure from [8].

extinction ratio is defined as the power generated when the laser is on divided by the power generated when the laser is off, or in terms of the EOM the ratio of the power generated at full transmission to the power generated at full suppression of light. For the ACS, we expect

$$\frac{P_{avg,ON}}{P_{avg,OFF}} \cong 10^{-3} = -30\,\text{dB}. \tag{3.9}$$

However, when the measurements of $P_{avg,ON}$ and $P_{avg,OFF}$ are shifted by a small DC voltage, like V_{OS}, this changes the ratio between them, if not the difference. For example, $\frac{A+\delta}{B+\delta} \neq \frac{A}{B}$, where $\frac{A}{B}$ is the ratio of some numbers and δ is a small offset added to both of them.

Due to this problem of dynamic range, it was important to develop a strategy to eliminate the offset voltage at the op amps in this revision of the LSB, and also to do so in a way that did not use too much space.

3.4.1 Offset Voltage

The offset voltage arises in non-ideal op amps. In an ideal op amp, when both input voltages are equal ($V_+ = V_-$), the output is zero. However, in real op amps, a small input offset voltage, V_{OS}, is required to ensure that $V_{out} = 0$. The offset voltage is physically represented as a separate voltage source in series with V_-, the inverting terminal of the op amp, as shown in Figure 3-15 [8].

For a simple inverting amplifier circuit as the one shown in Figure 3-16, we can use Ohm's Law, Kirchoff's Law, and the Golden Rules of op amps to relate V_{out} to V_{in} and show the effect of V_{OS} on the system.

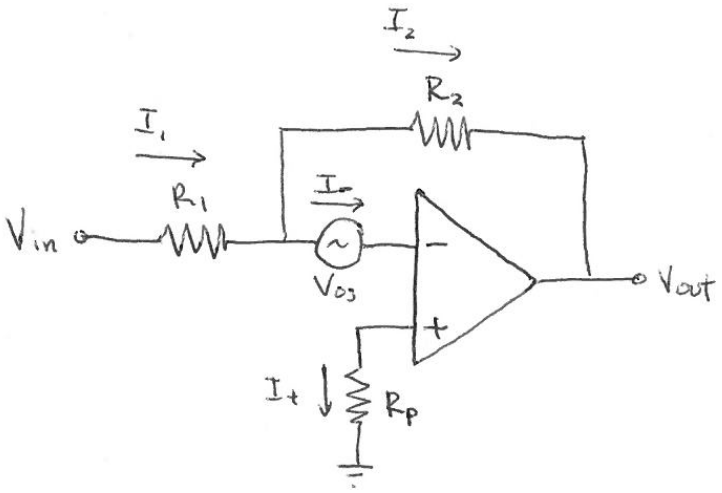

Figure 3-16: Non-ideal inverting amplifier with V_{OS}.

- $I_+ = 0$ [Golden Rule #2], therefore $\Delta V_{R_P} = 0$ and $V_+ = 0$.
- $V_- = V_+ = 0$ [Golden Rule #1]
- From Kirchoff's Current Law, $I_1 = I_2 + I_-$.
- $I_- = 0$ [Golden Rule #2]
- Then, $I_1 = I_2 = I$.
- $\Delta V_{R_1} = IR_1 = V_{in} - V_{OS}$ [Ohm's Law]
- $\Delta V_{R_2} = IR_2 = V_{OS} - V_{out}$ [Ohm's Law]
- Rearranging these two expressions and eliminating I gives us:

$$V_{out} = -\frac{R_2}{R_1}V_{in} + \left(\frac{R_2}{R_1} + 1\right)V_{OS} \tag{3.10}$$

In Equation 3.10, $-\frac{R_2}{R_1}$ is the signal gain, while $\left(\frac{R_2}{R_1}+1\right)$ is the noise gain, amplifying the offset voltage. Because it is generally not desirable to have the op amp amplify noise in addition to the signal, we consider the following circuit shown in Figure 3-17, in which a small offset voltage is injected into the non-inverting input to counteract the effect of the op amp's natural offset voltage. This configuration can be used to null

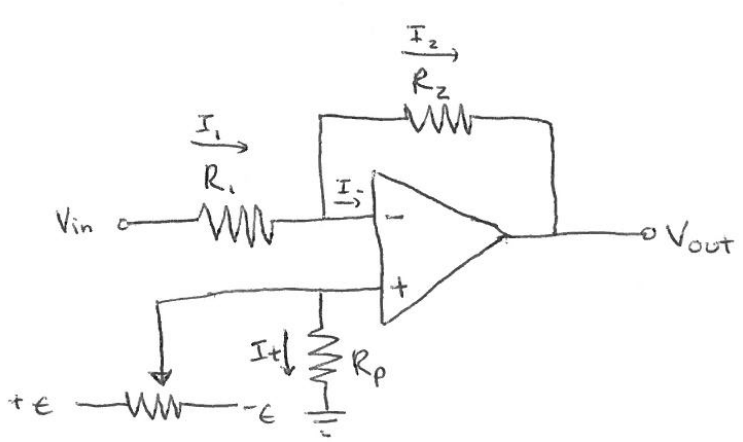

Figure 3-17: Inverting amplifier with small voltage $\pm\epsilon$ injected into V_+.

the noise gain from the offset voltage. Here, $\pm\epsilon$ is a small voltage created from a $\pm 5\,\mathrm{V}$ source and voltage dividers in a circuit shown in Figure 3-18. Resistors R_A and R_B can be chosen to create the appropriate $\pm\epsilon$ for a given system. The potentiometer separating $\pm\epsilon$ allows users to manually adjust the the small offset voltage that is being injected into V_+, which is important given that V_{OS} can vary over time and with temperature.

Once again, we can use Ohm's Law, Kirchoff's Law, and the Golden Rules of op amps to relate V_{out} to V_{in}.

- $V_+ = \pm\epsilon$
- $V_+ = V_- = \pm\epsilon$ [Golden Rule #1]
- From Kirchoff's Current Law, $I_1 = I_2 + I_-$.
- $I_- = 0$ [Golden Rule #2]
- Then, $I_1 = I_2 = I$.
- $\Delta V_{R_1} = IR_1 = V_{in} - (\pm\epsilon)$ [Ohm's Law]
- $\Delta V_{R_2} = IR_2 = (\pm\epsilon) - V_{out}$ [Ohm's Law]

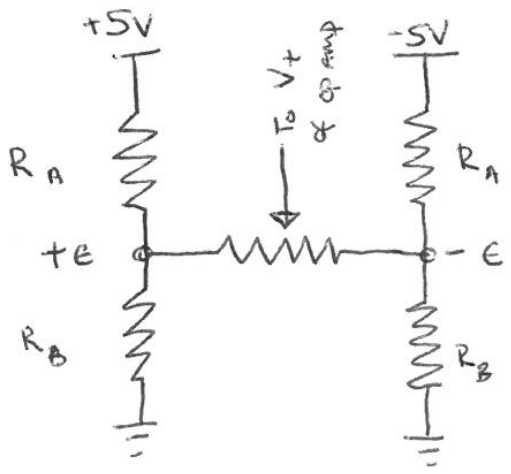

Figure 3-18: Circuit to create $\pm\epsilon$ from $\pm 5\,\mathrm{V}$ voltage sources using voltage dividers. Using $\pm\epsilon = \pm 5\,\mathrm{V} * R_B/(R_A + R_B)$, to ensure small ϵ, we require $R_A \gg R_B$.

- Rearranging and eliminating I gives:

$$V_{out} = -\frac{R_2}{R_1}V_{in} + \left(\frac{R_1}{R_2} + 1\right)(\pm\epsilon) \tag{3.11}$$

By adding this configuration of $\pm\epsilon$ to a circuit with an offset voltage, one can take advantage of the linearity of these voltage terms and adjust the potentiometer so that ϵ matches V_{OS}. This effectively cancels out the linear addition of the noise gain to V_{out}. One can apply this technique of injecting a small voltage $\pm\epsilon$ into the V_+ terminal of the op amp to APOLLO's more complicated op amp circuits, which will be discussed in Subsection 3.4.2.

3.4.2 Nulling V_{OS} in the LSB's Average Power Measurements

APOLLO's system is more complex than the simple inverting amplifier system described in Subsection 3.4.1, as it consists of two of these inverting amplifier circuits in series with each other. However, in the non-ideal system shown in Figure 3-19, V_{out} of the first inverting amplifier equals V'_{in}. Using Equation 3.10, it is then simple to

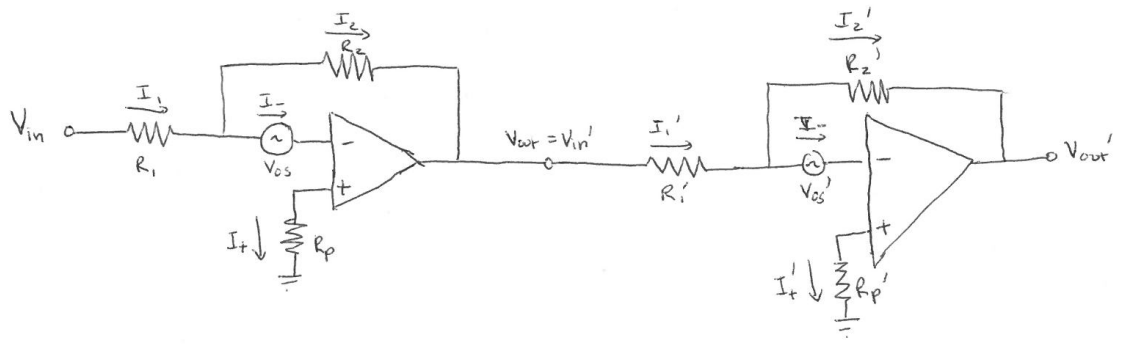

Figure 3-19: Two non-ideal inverting amplifiers with V_{OS} in series. In the case of LSB's average power circuit, the current I_1 through the resistor R_1 is equivalent to the current coming from the photodiode, I_{PD}.

find an expression relating V'_{out} to V_{in}.

$$\begin{aligned} V'_{out} &= -\frac{R'_2}{R'_1}V'_{in} + \left(\frac{R'_2}{R'_1}+1\right)V'_{OS} \\ &= -\frac{R'_2}{R'_1}\left[-\frac{R_2}{R_1}V_{in} + \left(\frac{R_2}{R_1}+1\right)V_{OS}\right] + \left(\frac{R'_2}{R'_1}+1\right)V'_{OS} \\ &= \frac{R_2R'_2}{R_1R'_1}V_{in} - \frac{R'_2}{R'_1}\left(\frac{R_2}{R_1}+1\right)V_{OS} + \left(\frac{R'_2}{R'_1}+1\right)V'_{OS} \end{aligned} \tag{3.12}$$

Now, we have two noise terms in the expression for V'_{out} giving a gain to both offset voltages, V_{OS} and V'_{OS} that we need to nullify. While it is possible to use the method described in Subsection 3.4.1, and inject a small voltage into the non-inverting terminals of both of the op amps, this is not desirable because it comes with a sacrifice of space. The resistor configuration, and particularly the potentiometer required to vary the small voltage, ϵ, take up a non-trivial part of the board, which already is quite tight for space.

However, it is possible to null both offset voltages by injecting an offset voltage, ϵ, into only the V_+ terminal of the first op amp, a design consideration that has been taken into account in the second revision of the LSB. In this case we can consider the

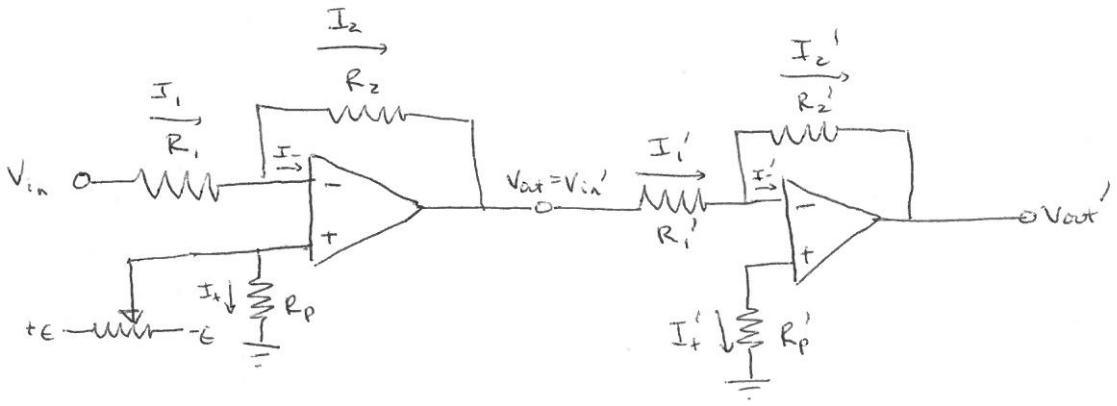

Figure 3-20: Two inverting amplifiers with with a small voltage $\pm\epsilon$ injected into the V_+ terminal of the first op amp. I_1 is equivalent to I_{PD} in the LSB's average power circuit.

circuit depicted in Figure 3-20. For this circuit, the relation of V'_{out} to V_{in} is then:

$$\begin{aligned} V'_{out} &= -\frac{R'_2}{R'_1}V'_{in} \\ V'_{out} &= -\frac{R'_2}{R'_1}\left[-\frac{R_2}{R_1}V_{in} + \left(\frac{R_2}{R_1}+1\right)(\pm\epsilon)\right] \\ V'_{out} &= \frac{R_2R'_2}{R_1R'_1}V_{in} - \frac{R'_2}{R'_1}\left(\frac{R_2}{R_1}+1\right)(\pm\epsilon) \end{aligned} \tag{3.13}$$

To null the offset voltages, we require,

$$-\frac{R'_2}{R'_1}\left(\frac{R_2}{R_1}+1\right)V_{OS} + \left(\frac{R'_2}{R'_1}+1\right)V'_{OS} = -\frac{R'_2}{R'_1}\left(\frac{R_2}{R_1}+1\right)(\pm\epsilon) \tag{3.14}$$

or

$$\pm\epsilon = V_{OS} - \frac{R'_1}{R'_2}\frac{\left(\frac{R'_2}{R'_1}+1\right)}{\left(\frac{R_2}{R_1}+1\right)}V'_{OS}. \tag{3.15}$$

We want to determine ϵ for the worst case scenario because the potentiometer gives us flexility in the voltage range $V < |\pm\epsilon|$. For the AD824 op amp used by APOLLO, the specification for the maximum V_{OS} is 1.5 mV when biased with $V_S = 5\,\mathrm{V}$, and we round this up to 2 mV to add a buffer. Since the op amps are identical in the average power measurement and V_{OS} can be both positive and negative voltages, we

set $V'_{OS} = -V_{OS} = 2$ mV, the worst case scenario. Using the resistor values from Figure 3-10, we give the following values for the resistors specified in Equation 3.15:

- $R_1 = 500\,\Omega$ (not shown in Figure 3-10)
- $R_2 = 20\,\text{k}\Omega + 50\,\text{k}\Omega = 70\,\text{k}\Omega$, where $50\,\text{k}\Omega$ is the maximum value of the potentiometer.
- $R'_1 = 10\,\text{k}\Omega$
- $R'_2 = 100\,\text{k}\Omega$

When we input these values into Equation 3.15, we find $|\pm\epsilon| = 2.02$ mV. We can then determine the values of the resistors R_A and R_B from Figure 3-18 that would create the appropriate $\pm\epsilon$ from the ± 5 V supply. Using the expression for the output voltage of a voltage divider, we have $\pm\epsilon = \pm 5\,\text{V} * R_B/(R_A + R_B)$. Inputting our calculated value of ϵ gives us the ratio:

$$\begin{aligned} \frac{\pm\epsilon}{\pm 5\,\text{V}} &= \frac{R_B}{(R_A + R_B)} \\ 4.03 \times 10^{-4}\,\text{V} &= \frac{R_B}{(R_A + R_B)} \end{aligned} \tag{3.16}$$

Rearranging, we determine the relation:

$$\frac{R_A}{R_B} = \frac{1 - x}{x} = 2.48 \times 10^3 \tag{3.17}$$

where x is the ratio of ϵ to 5 V, or $\frac{\epsilon}{5\,\text{V}} = 4.03 \times 10^{-4}\,\text{V}$. We find that we require the resistor R_A to be about 2500 times larger than R_B in order to provide an appropriate value of ϵ to our circuit.

3.5 Summary

In this chapter, we have developed the theory behind the ACS and the motivations for its implementation at APOLLO to provide a groundwork for the second round of

revisions to the LSB. In particular, we have determined a technique to eliminate the problem of dynamic range that occurred in the first version. We have shown that it is possible to null the effect of the offset voltage from the two op amps in the average power measurement through a single circuit.

Chapter 4

Gravitational Redshift

APOLLO employs two different clocks during data collection: one associated with the measurement of the Earth-Moon travel time of a photon and the other with the ACS, or Absolute Calibration System. A Symmetricon XL-DC model clock is employed for the Earth-Moon travel time measurements, and is GPS-disciplined so that the clock acts as if it were at "sea level" [13]. The other clock, a 5071A cesium clock from Microsemi (formerly Symmetricon), acts as a reference for the high-frequency laser pulses used for accuracy calibration [5]. While both are on-site, the GPS-disciplined clock acts as if it were 2.8 km lower in altitude, so we can call the XL-DC clock the "sea level" clock, and the cesium clock the "high altitude" clock. Because the clocks act as though they were at two different gravitational potentials, time measurements from APOLLO data can reveal the effects of a change of gravitational potential on time.

4.1 GPS Network of Clocks

Global Positioning System disciplined oscillators (GPSDO or GPS-disciplined clock) have become much more commomly employed as frequency standards in the recent years, including at APOLLO as the primary frequency standard. While traditionally frequency standards consisted of quartz, rubidium, or cesium oscillators, with rubidium and cesium being the more costly yet better performing options of the

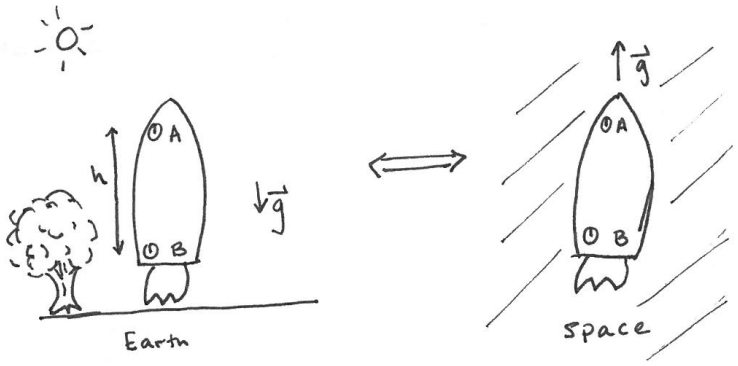

Figure 4-1: A depiction of the equivalence principle. Clocks in a rocket on earth experiencing a local gravitational acceleration are equivalent to clocks in a rocket in space accelerating at the same rate. Figure based on diagram in [9].

three, GPSDOs provide a fourth quartz- or rubidium-based oscillator alternative often cheaper than a cesium oscillator, with a frequency controlled by GPS satellites. The GPS satellites, under the operation of the U.S. Deptartment of Defense, provide a frequency reference used across the globe through the atomic oscillators they each carry. These atomic oscillators are synced to the Coordinated Universal Time maintained by the United States Naval Observatory, UTC(USNO), one of the primary time standards worldwide [18]. This frequency standard is maintained at sea level, causing the GPS-disciplined clock at APOLLO to act as if it were also at sea level.

GPSDOs are highly accurate and reliable both because of the atomic oscillators at the core of the system and the accuracy required of GPS itself to function as positioning network. Generally, GPS positioning is required to be within a meter of its intended position. Using $3 \times 10^8\,\mathrm{m\,s^{-1}}$ as the speed of light, the equivalent uncertainty in time is 3.3 ns. Thus a high level of stablity is required of the atomic clocks on the GPS satellites, so that they can maintain an error less than 3.3 ns in the period between corrections from UTC(USNO) [18].

4.2 Theory

Following the derivation in Hartle's textbook, we can determine the gravitational redshift between two objects in the weak-field limit of gravity, which is applicable at

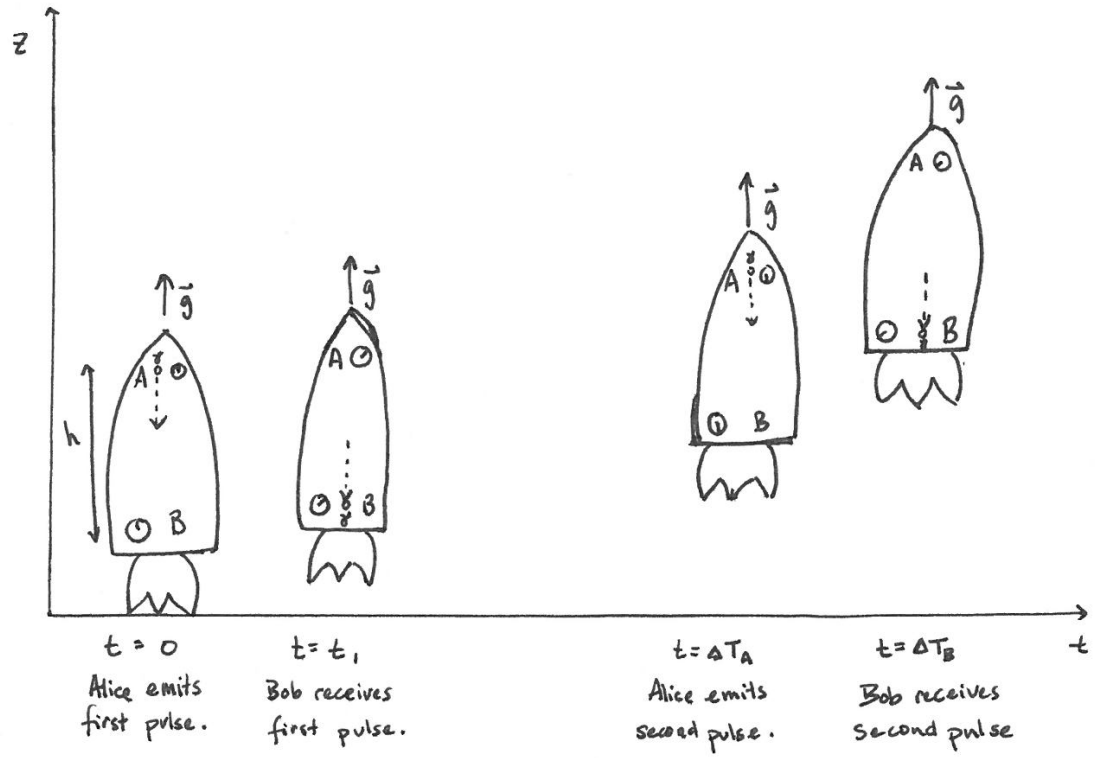

Figure 4-2: The positions of the rocket as Alice and Bob send and receive pulses of light. The second pulse of light travels a shorter distance than the first pulse due to the acceleration of the rocket, and as a result Bob measures a shorter time interval between the two pulses. Figure based on diagram in [9].

the Earth's surface and for the two clocks used by APOLLO [9]. Shown in Figure 4-1, by the equivalence principle, the two clocks in a gravitational field both experiencing a local acceleration of $-\mathbf{g}$ is the equivalent to two clocks in a rocket accelerating at $\mathbf{g}$ through empty space. We are further ignoring any effect of special relativity under the assumption that the rocket does not reach relativistic velocities in the time intervals we are comparing. This implies that $(gh/c^2)^2$ is negligible, so Newtonian mechanics are valid. To begin, we can imagine one clock A to be at the tip of a rocket of height h read by "Alice" and another, clock B, at the base of the rocket that is read by "Bob." Then the respective positions of clock A and clock B as a function of time are

$$z_A(t) = h + \frac{1}{2}gt^2 \tag{4.1}$$

and

$$z_B(t) = \frac{1}{2}gt^2. \tag{4.2}$$

To analyze the difference in time measurements made by Alice and Bob, we can look at what happens if Alice sends two pulses of light to Bob in the accelerating spaceship. If Alice sends the first pulse of light to Bob at $t = 0$, then Bob will receive it at some time t_1. The distance traveled by the first pulse is then

$$z_A(0) - z_B(t_1) = ct_1. \tag{4.3}$$

If Alice sends another pulse of light at ΔT_A and Bob receives it at $t_1 + \Delta T_B$, its path will be shorter than the first pulse's path due to the acceleration of the rocket, as shown in Figure 4-2. The path of the second pulse is given by the following expression:

$$z_A(\Delta T_A) - z_B(t_1 + \Delta T_B) = c(t_1 + \Delta T_B - \Delta T_A). \tag{4.4}$$

From here, we can substitute in Equations 4.1 and 4.2, ignoring any non-linear terms in ΔT_A and ΔT_B, since they are sufficiently small. This gives

$$h - \frac{1}{2}gt^2 = ct_1, \tag{4.5a}$$

$$h - \frac{1}{2}gt^2 - gt_1\Delta T_B = c(t_1 + \Delta T_B - \Delta T_A). \tag{4.5b}$$

Manipulating these two equations and substituting t_1 to the first order approximation $t_1 = h/c$ gives the following relation between ΔT_A and ΔT_B:

$$\Delta T_B = \Delta T_A\left(1 - \frac{gh}{c^2}\right). \tag{4.6}$$

This result tells us that Bob measures a time interval between the two pulses he receives smaller by a factor of $(1 - gh/c^2)$ than the time interval that Alice sends the two light pulses.

Also important to consider are the rates of emission and reception of the light pulses, or $1/\Delta T_A$ and $1/\Delta T_B$ respectively. This is simply the inverse of Equation 4.6, and taking into account that $gh/c^2 \ll 1$, so the binomial approximation can be used,

$$\frac{1}{\Delta T_B} = \frac{1}{\Delta T_A}\left(1 + \frac{gh}{c^2}\right) \tag{4.7}$$

Thus Bob receives light at a higher frequency than Alice emits it.

Recognizing that gh is the change in gravitational potential in a uniform gravitational field, we can apply this analysis to the surface of the earth, which has an approximately uniform gravitational field. If we let $\Phi_A - \Phi_B$ be the change of gravitational potential from points B to A, then we can rewrite Equation 4.6 as

$$\Delta T_B = \Delta T_A\left(1 - \frac{\Phi_A - \Phi_B}{c^2}\right). \tag{4.8}$$

In a situation where point A is at a higher altitude than point B with a difference of altitude h, we regain Equation 4.6 and find that a clock at a higher gravitational potential, or a higher altitude, will measure more time relative to the clock at a lower

potential.

As time goes on, the difference in time measurements between these two clocks will increase linearly with respect to time. We can manipulate Equation 4.6 to find the rate of change of ΔT, the time difference between the two clocks. The expression is as follows:

$$\frac{\Delta T}{T_A} = \frac{T_B - T_A}{T_A} = \frac{gh}{c^2}. \tag{4.9}$$

4.3 Analysis of APOLLO Data

Since January 2016, APOLLO has been actively measuring the change in its two very stable clocks, the "high altitude" cesium clock and "sea level" GPS-disciplined clock [19]. By plotting change in time, ΔT, as a function of time, we can compare the experimental data to theoretical expectations for gravitational redshift at Apache Point (2.8 km above sea level). Using Equation 4.9, we can determine the slope of the linear relationship between time and the change in time between APOLLO's two clocks. For an altitude of $h = 2.8\,\mathrm{km}$, we would expect the slope of the line due to gravitational redshift to be $\frac{\Delta T}{T_A} = 26\,\mathrm{ns\,d^{-1}}$. However, our cesium clock is not ideal and according to the manufacturer runs slow by $11\,\mathrm{ns\,d^{-1}}$ as measured against a hydrogen maser, a much more stable clock. Taking this into account, we would instead expect the slope of the line to be $26\,\mathrm{ns\,d^{-1}} - 11\,\mathrm{ns\,d^{-1}} = 15\,\mathrm{ns\,d^{-1}}$.

Looking at Figure 4-3, we see the experimental data generally follow this prediction. There are some notable exceptions. First, there are piecewise jumps in the data. This is due to APOLLO's proximity to White Sands Missile Range in New Mexico. Periodically, GPS jamming activities at the Missile Range interfere with the APOLLO GPS clock causing it to stop and reset. This causes small leaps in the relative difference between the GPS-disciplined clock and the cesium clock, which is unaffected by the GPS jamming.

Even with the disruptions to the GPS-disciplined clock, we would expect the piecewise parts of the figure to have the same slope. However, the slope appears to be shallower at late times ($t > 150\,\mathrm{d}$) than at early times, where it does align

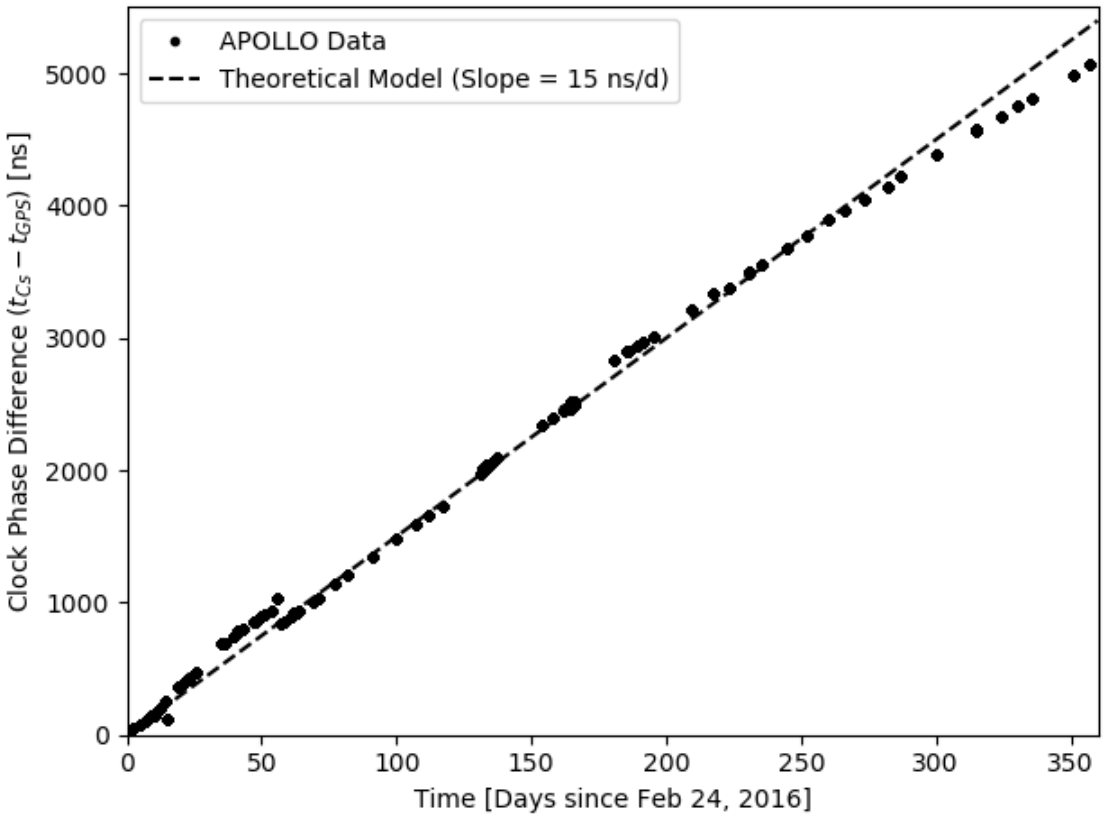

Figure 4-3: Time difference between APOLLO's cesium "high altitude" clock and GPS-disciplined "sea level" clock as a function of time compared with theoretical expectation of the relationship.

relatively well with the theoretical slope. This deviation of the slope is something we discovered in the process of doing this analysis, and we are still investigating its cause.

Chapter 5

Conclusion

Over the course of this thesis, I have explored a breadth of both theoretical and experimental aspects of APOLLO operations and relativistic gravity.

The opto-tilt board I designed, populated, and tested is now part of routine APOLLO operation at the Apache Point Observatory. In addition, we have finished the schematic and layout of a third revision to the opto-tilt board, and the next steps include populating and then installing the board over the summer at Apache Point Observatory.

The scope of my work for this thesis centered around understanding the theory behind the LSB, and by extension the ACS, so as to be able to make revisions to the first version of the schematic of the LSB. In particular, we showed that we can correct the offset voltage of two op amps with a single circuit, as outlined in Section 3.4. However, there is still much to do before we install a second revision of the LSB at Apache Point Observatory. Future goals encompass updating the layout of the LSB to include changes from the schematic, printing and populating the board, and performing table-top tests of the board using the high-frequency fiber laser at Wellesley. Once all this has been accomplished, we can then install the board at APOLLO, likely in the summer of 2017. In addition to completing the second revision to the LSB, a paper on the ACS that I am co-authoring is currently in preparation for submission to *Classical and Quantum Gravity*.

Finally, the theoretical analysis of gravitational redshift and its application to

APOLLO's time measurement data show a general trend as expected. However, we are still considering possible causes for an unexpected deviation in the slope, $\Delta t/t$, at late times, as discussed in Section 4.3.

Appendix A

Figures

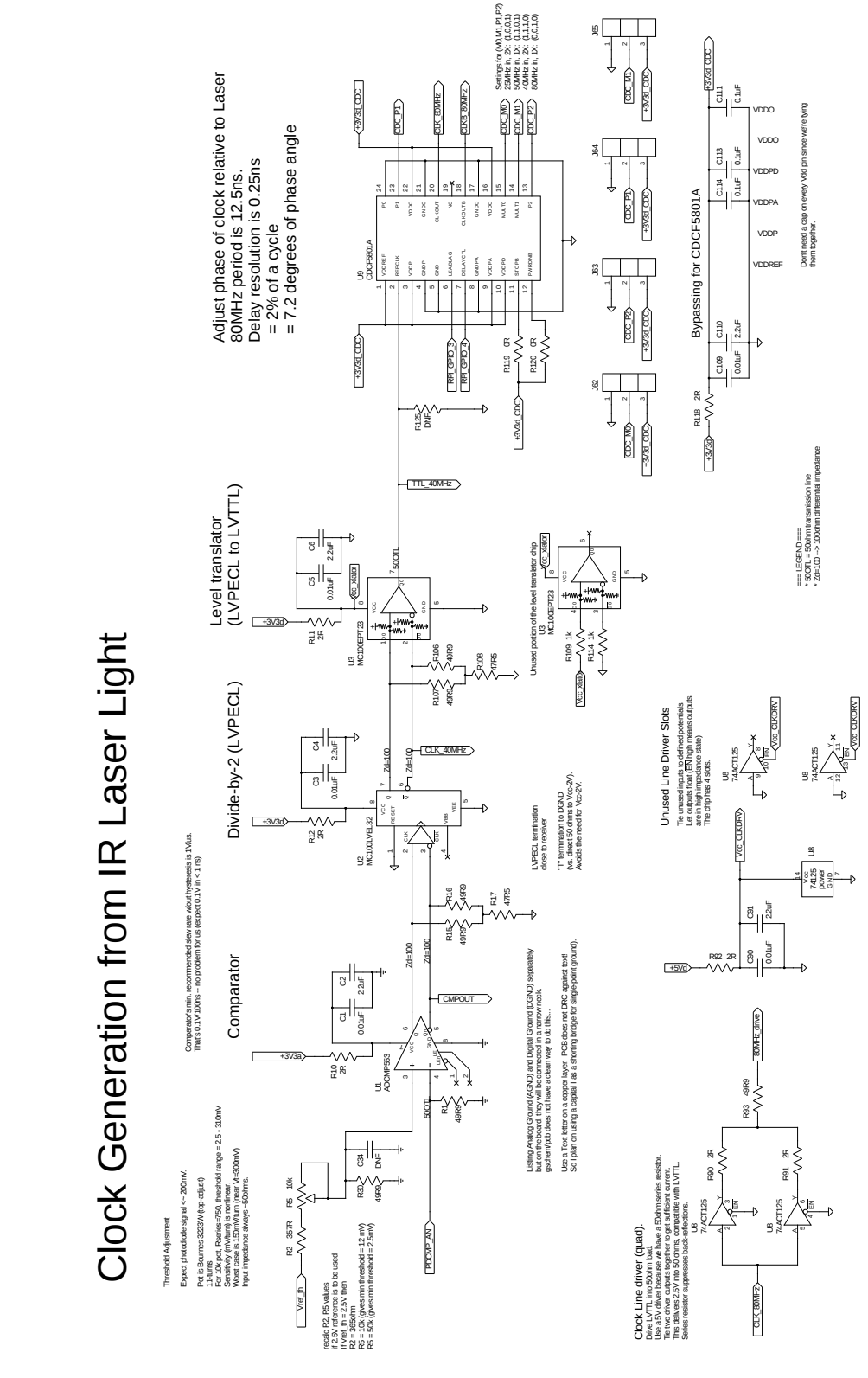

Figure A-1: LSB schematic: clock generation.

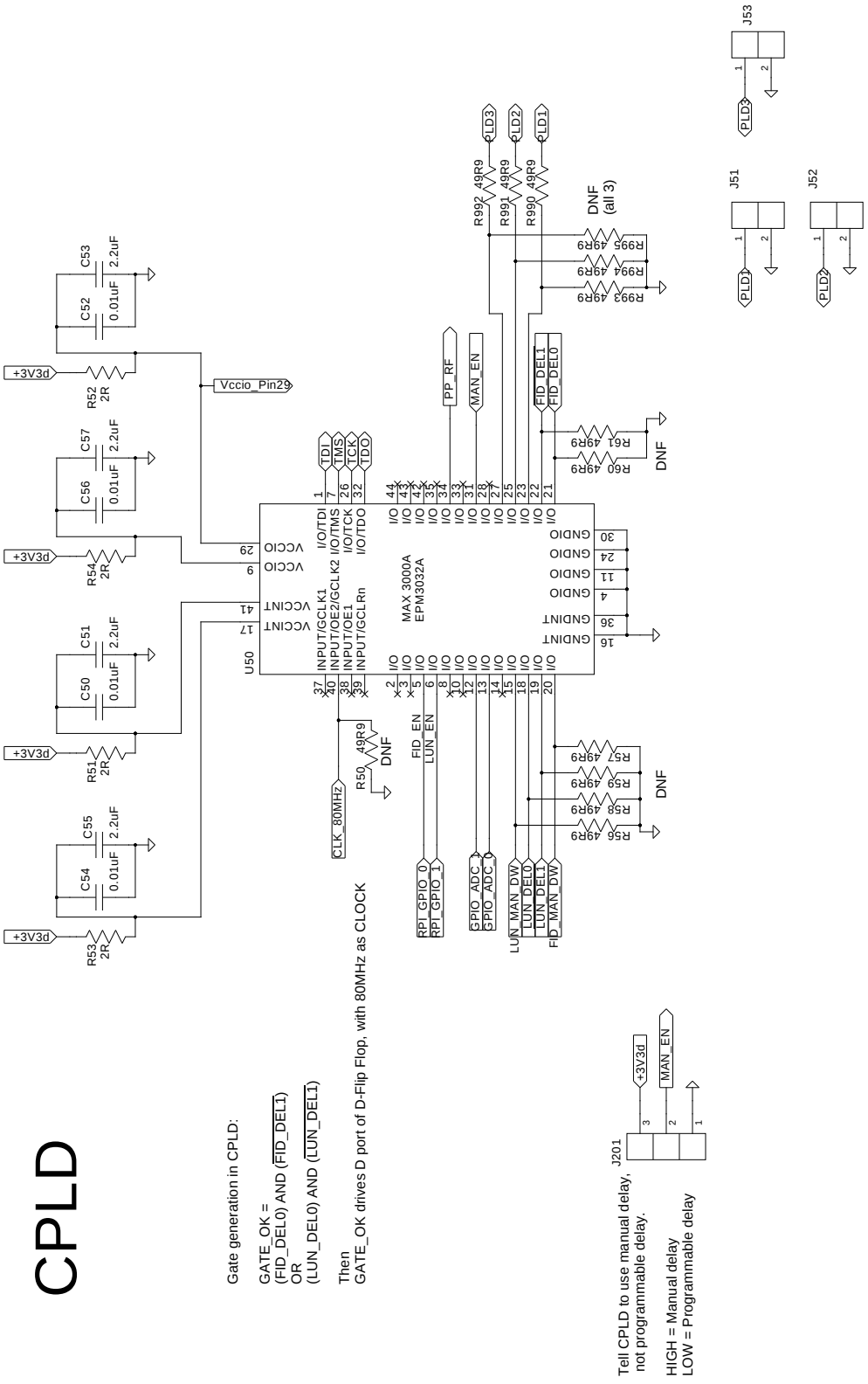

Figure A-2: LSB schematic: CPLD.

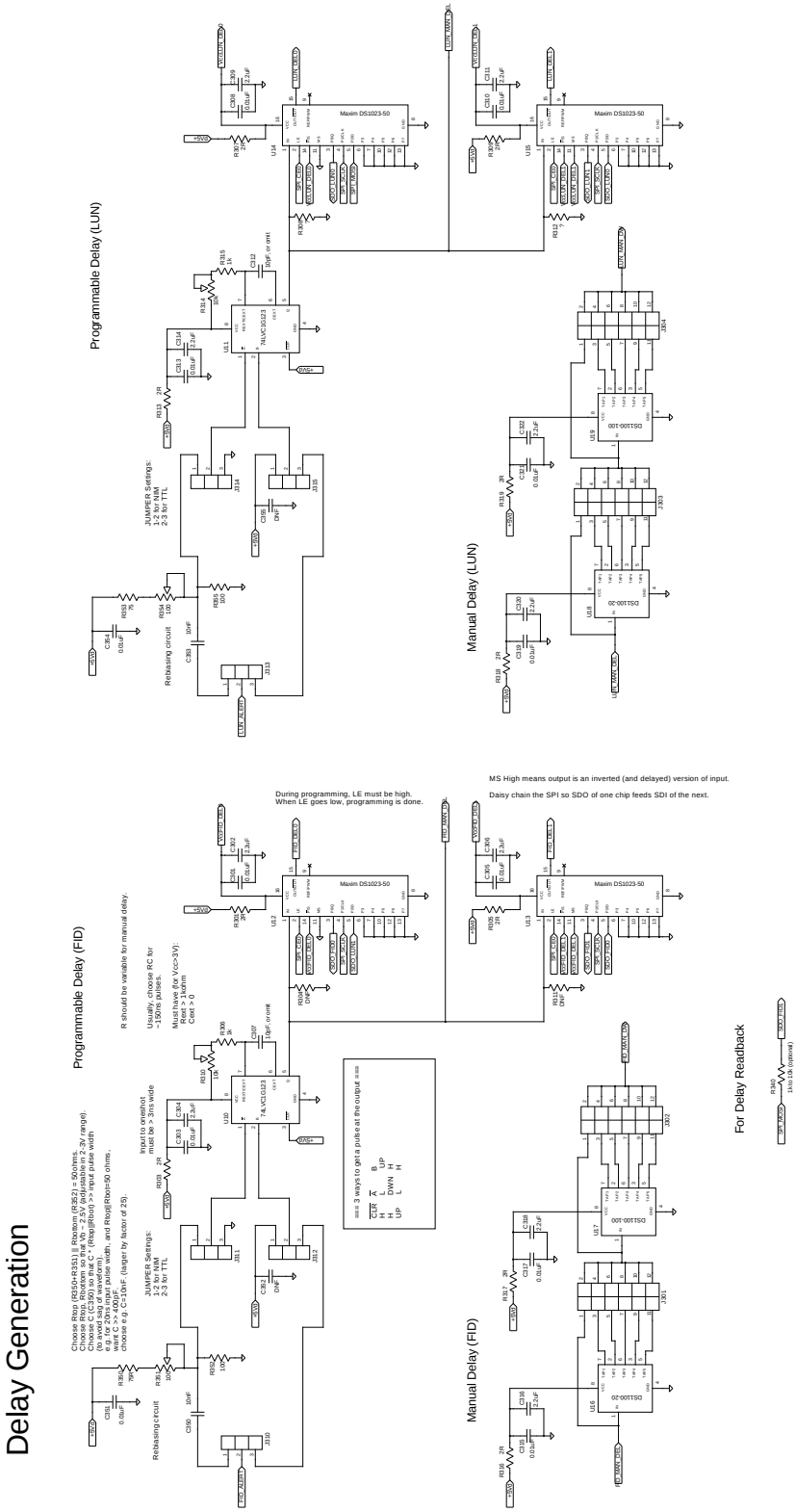

Figure A-3: LSB schematic: delay generation.

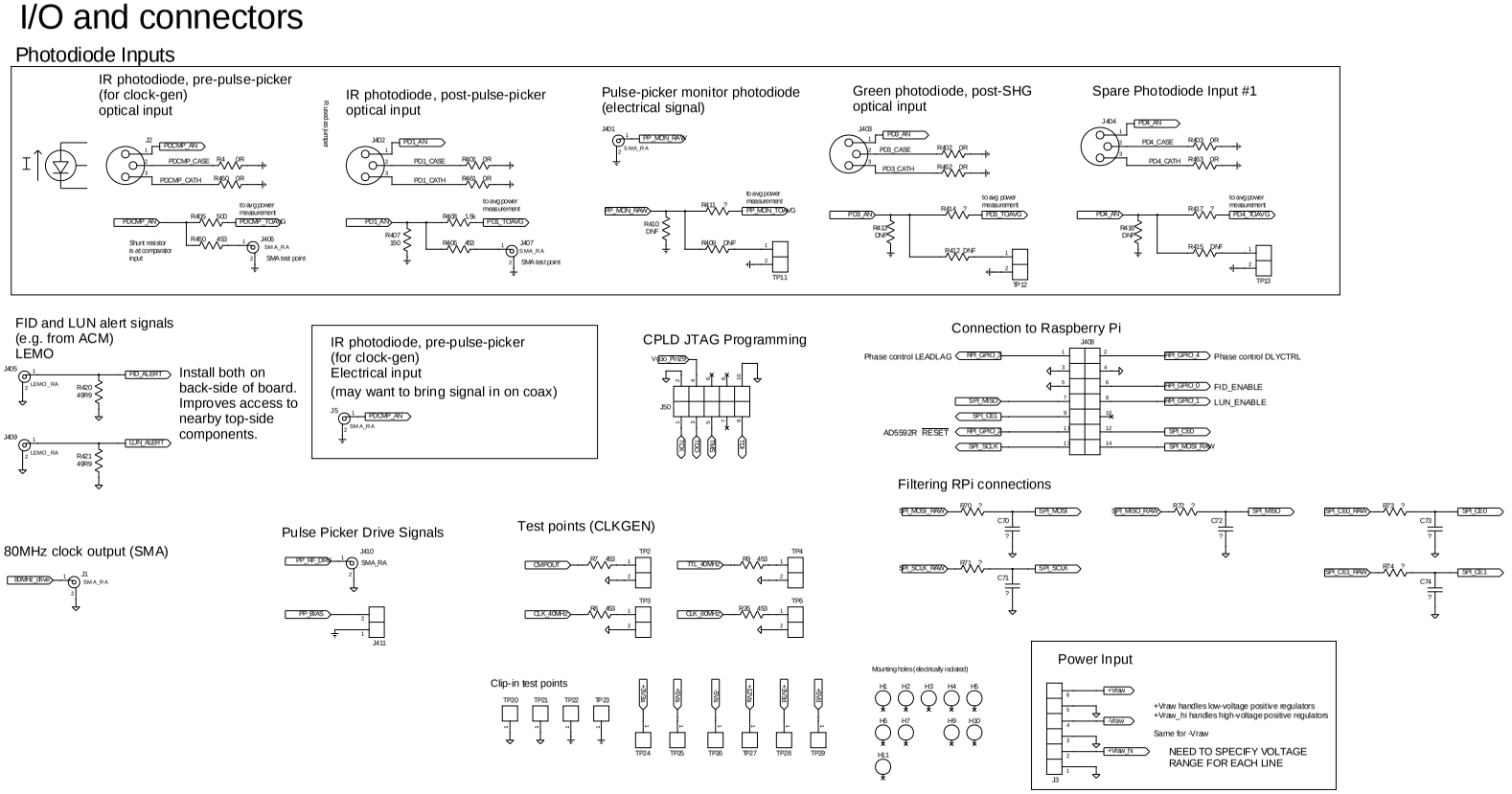

Figure A-4: LSB schematic: I/O and connectors.

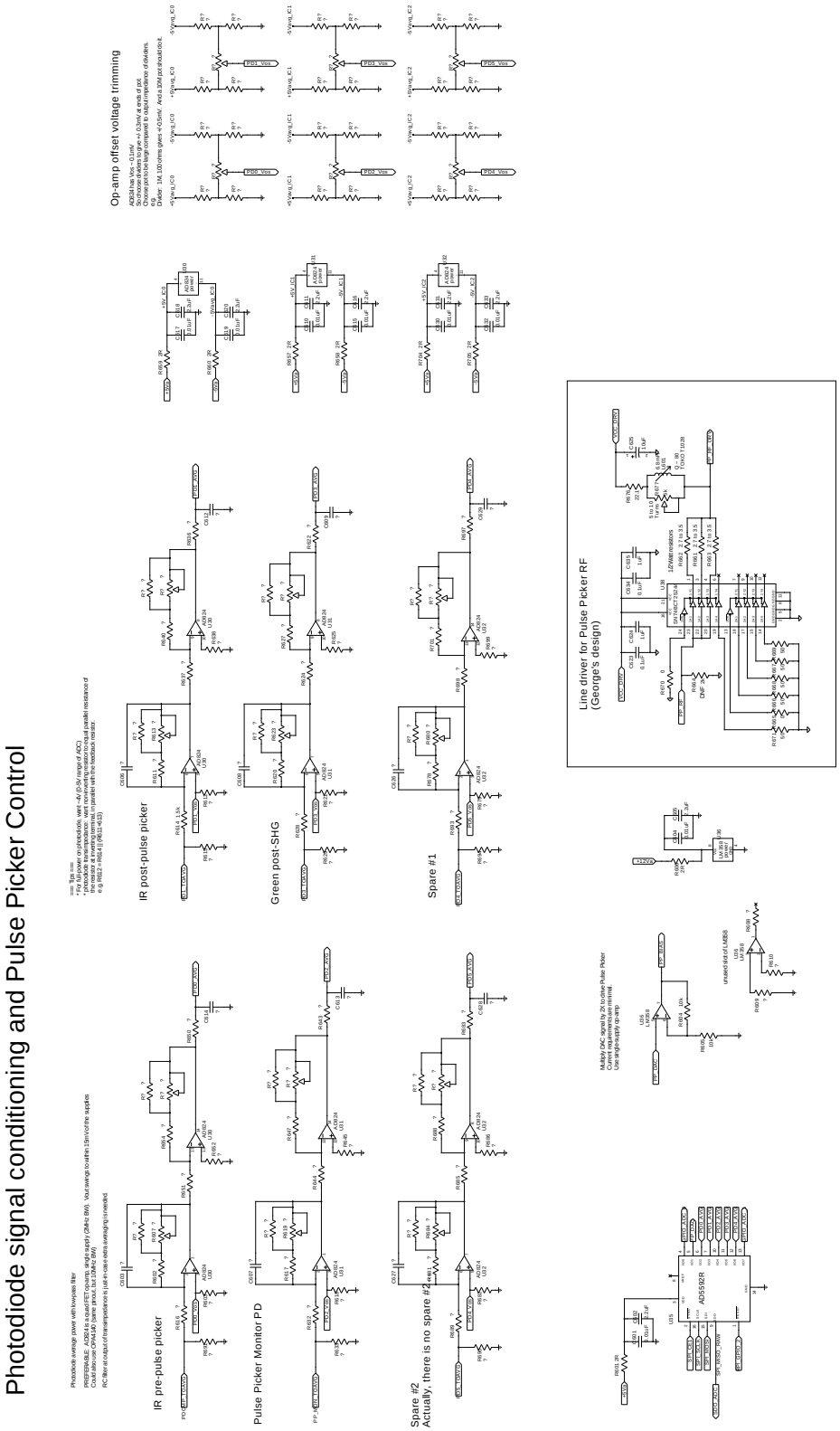

Figure A-5: LSB schematic: photodiode average power measurement and pulse picker.

Figure A-6: LSB schematic: power supplies.

Power Supplies

Analog

+3.3V supply for analog: comparator

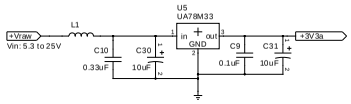

+/-5V supply for analog: ADC/DAC, PD op-amps

These +/-5V regulators must be >1A, so use the D2PAK footprint.

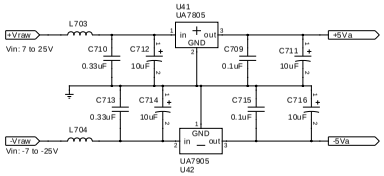

+12V supply for analog: DAC 2X multiplier

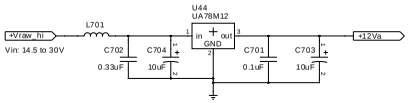

Digital

+3.3V supply for digital: clockgen, CPLD

There are plenty of 1.5A 3.3V regulators in the DPAK footprint (but NOT called 7833). See e.g. LD1086, LD3915, etc.

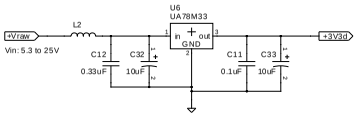

+5V supply for digital: Line Drivers, Delay Chips

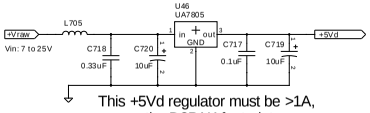

This +5Vd regulator must be >1A, so use the D2PAK footprint.

Adjustable supply for digital: Line driver for PP RF

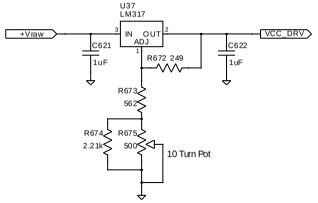

+5V reference for CLKGEN comparator threshold

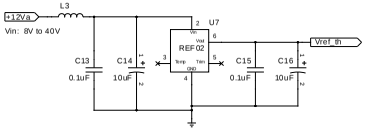

Could actually use a lower reference voltage than +5V.
e.g. the 2.5V reference (AD REF03).
In fact, new designs should use ADR01/02/03/06
Pin-for-pin compatible with the REFXX series.

NOTE:
To connect AGND and DGND on the pcb, use the copper text kludge.
Insert a (e.g.) capital letter "I", or several side-by-side

Bypass capacitors for ICs are to be placed on the relevant signal sheet. NOT here.

Bibliography

[1] T. W. Murphy. Lunar laser ranging: the millimeter challenge. *Reports on Progress in Physics*, 76(7):076901, July 2013.

[2] J. G. Williams, S. G. Turyshev, and D. H. Boggs. Lunar Laser Ranging Tests of the Equivalence Principle with the Earth and Moon. *International Journal of Modern Physics D*, 18:1129–1175, 2009.

[3] ADXL335 - 5V ready triple-axis accelerometer (+-3g analog out). `https://www.adafruit.com/products/163`.

[4] Precision vs Accuracy Diagram. `http://kaffee.50webs.com/Science/images/Accuracy-vs-precision1.jpg`.

[5] ACS manual. *APOLLO internal memo*, 2016.

[6] Analog Devices Tutorial MT-038: Op Amp Input Bias Current. `http://www.analog.com/media/en/training-seminars/tutorials/MT-038.pdf`.

[7] P. Horowitz and W. Hill. *The Art of Electronics*. Cambridge University Press, 3 edition, 2015.

[8] Analog Devices Tutorial MT-037: Op Amp Input Offset Voltage. `http://www.analog.com/media/en/training-seminars/tutorials/MT-037.pdf`.

[9] James B. Hartle. *Gravity: An Introduction to Einstein's General Relativity*. Addison Wesley, 2003.

[10] Resolution of Contradictions. `http://www.theory.caltech.edu/people/jhs/strings/string11.html`. Accessed: 2017-01-20.

[11] LIGO Lab — Caltech. `https://www.ligo.caltech.edu/page/learn-more`. Accessed: 2017-01-20.

[12] J. B. R. Battat, T. W. Murphy, E. G. Adelberger, B. Gillespie, C. D. Hoyle, R. J. McMillan, E. L. Michelsen, K. Nordtvedt, A. E. Orin, C. W. Stubbs, and H. E. Swanson. The Apache Point Observatory Lunar Laser-ranging Operation (APOLLO): Two Years of Millimeter-Precision Measurements of the Earth-Moon Range. *Publ. Astro. Soc. Pacific*, 121:29, January 2009.

[13] T. W. Murphy, Jr., E. G. Adelberger, J. B. R. Battat, L. N. Carey, C. D. Hoyle, P. LeBlanc, E. L. Michelsen, K. Nordtvedt, A. E. Orin, J. D. Strasburg, C. W. Stubbs, H. E. Swanson, and E. Williams. The Apache Point Observatory Lunar Laser-ranging Operation: Instrument Description and First Detections. *Publ. Astro. Soc. Pacific*, 120:20, January 2008.

[14] T. W. Murphy, Jr., E. G. Adelberger, J. B. R. Battat, C. D. Hoyle, N. H. Johnson, R. J. McMillan, C. W. Stubbs, and H. E. Swanson. APOLLO: millimeter lunar laser ranging. *Classical and Quantum Gravity*, 29(18):184005, September 2012.

[15] Susan Brown. Source of 'Moon Curse' Revealed by Eclipse. `http://ucsdnews.ucsd.edu/feature/source_of_moon_curse_revealed_by_eclipse`, Feb 2014.

[16] H11L1 Fairchild Semiconductor Datasheet. `https://www.fairchildsemi.com/datasheets/H1/H11L1M.pdf`.

[17] T. W. Murphy, Jr., J. B. R. Battat, N. Colmenares, E. G. Adelberger, C. D. Hoyle, L. Huang Ruixue, E. Schlerman, and C. W. Stubbs. Achieving millimeter precision in lunar laser ranging. *manuscript in preparation for submission to Classical and Quantum Gravity*, 2017.

[18] M. A. Lombardi. The Use of GPS Disciplined Oscillators as Primary Frequency Standards for Calibration and Metrology Laboratories. *NCSCI Measure*, September 2008.

[19] J. B. R. Battat and E. Schlerman. Testing Einstein with a clock and a mountain. *submitted to the Wellesley College Journal of Science*, 2017.